



## Coarse-Grained Reduction and Analysis of a Network Model of Cortical Response: I. Drifting Grating Stimuli

MICHAEL SHELLEY AND DAVID McLAUGHLIN

*Courant Institute of Mathematical Sciences and Center for Neural Science, New York University,  
New York, NY 10012*  
shelley@cims.nyu.edu

*Received July 6, 2001; Revised December 21, 2001; Accepted February 19, 2002*

Action Editor: Bard Ermentrout

**Abstract.** We present a reduction of a large-scale network model of visual cortex developed by McLaughlin, Shapley, Shelley, and Wielaard. The reduction is from many integrate-and-fire neurons to a spatially coarse-grained system for firing rates of neuronal subpopulations. It accounts explicitly for spatially varying architecture, ordered cortical maps (such as orientation preference) that vary regularly across the cortical layer, and disordered cortical maps (such as spatial phase preference or stochastic input conductances) that may vary widely from cortical neuron to cortical neuron. The result of the reduction is a set of nonlinear spatiotemporal integral equations for “phase-averaged” firing rates of neuronal subpopulations across the model cortex, derived asymptotically from the full model without the addition of any extra phenomenological constants. This reduced system is used to study the response of the model to drifting grating stimuli—where it is shown to be useful for *numerical investigations* that reproduce, at far less computational cost, the salient features of the point-neuron network and for *analytical investigations* that unveil cortical mechanisms behind the responses observed in the simulations of the large-scale computational model. For example, the reduced equations clearly show (1) phase averaging as the source of the time-invariance of cortico-cortical conductances, (2) the mechanisms in the model for higher firing rates and better orientation selectivity of simple cells which are near pinwheel centers, (3) the effects of the length-scales of cortico-cortical coupling, and (4) the role of noise in improving the contrast invariance of orientation selectivity.

**Keywords:** visual cortex, neuronal networks, coarse-graining, dynamics, orientation selectivity, analysis

### 1. Introduction

Many neurons in the mammalian primary visual cortex respond preferentially to the particular orientation of elongated visual stimuli such as edges, bars, or gratings. So-called simple cells can act as nearly linear transducers of such visual stimuli and respond preferentially to spatial phase information. These selectivities, and others, are the bases for visual perception. The neural mechanisms that underly them remain in debate and are the object of both theoretical and experimental investigations (for a recent review, see Sompolinsky

and Shapley, 1997). There are many important and as yet unsettled foundational issues. These include the nature of the geniculate input to cortex, the origin of ordered (and disordered) “cortical maps” (such as orientation preference or retinotopy), the nature and specificity of the cortical architecture, the importance of feed-forward versus reciprocal coupling, the relative weights of cortical excitation and inhibition, sources of randomness, and the role of feed-back among the laminae of V1, with the lateral geniculate nucleus (LGN), and with higher visual areas.

In recent work we have developed a large-scale computational model of an input layer of the macaque primary visual cortex (V1), for the purpose of studying cortical response. The model describes a small local patch (1 mm<sup>2</sup>) of the cortical layer 4C $\alpha$ , which receives direct excitatory input from the LGN, and that contains four orientation hypercolumns with orientation pinwheel centers. In McLaughlin et al. (2000), we show that the model qualitatively captures the observed selectivity, diversity, and dynamics of orientation tuning of neurons in the input layer, under visual stimulation by both drifting and randomly flashed gratings (Ringach et al., 1997, 2001). In Wielaard et al. (2001), we show that remarkably for a nonlinear network, the model also captures the well known and important linear dependence of simple cells on visual stimuli, in a manner consistent with both extracellular (De Valois et al., 1982) and intracellular (Jagadeesh et al., 1997; Ferster et al., 1996) measurements. In Shelley et al. (2001), we show that cortical activity places our computational model cortex in a regime of large conductances, primarily inhibitory, consistent with recent intracellular measurements (Borg-Graham et al., 1998; Hirsch et al., 1998; Anderson et al., 2000).

This model instantiates a particular conception of the cortical network that is consistent with current understanding of cortical anatomy and physiology. The cortical network is taken as being two-dimensional and coupled isotropically and nonspecifically on subhypercolumn scales (<1 mm), with the length-scale of monosynaptic inhibition smaller than that of excitation (Fitzpatrick et al., 1985; Lund, 1987; Callaway and Wiser, 1996; Callaway, 1998; Das and Gilbert, 1999) and with cortico-cortical inhibition dominating cortico-cortical excitation (in simple cells). The cortex receives LGN input, weakly tuned for orientation, from a diverse set of segregated subregions of on- and off-center cells (Reid and Alonso, 1995). As is suggested by optical imaging and physiological measurement, the orientation preference set in the LGN input forms orientation hypercolumns, in the form of pinwheel patterns, across the cortex (Bonhoeffer and Grinvald, 1991; Blasdel, 1992). The LGN input also confers a preferred spatial phase, which varies widely from cortical neuron to cortical neuron (DeAngelis et al., 1999).

Cortical models have been used to show how orientation selectivity could be produced in cortex, based on “center-surround” interactions in the orientation domain (Ben-Yishai et al., 1995; Hansel and Sompolinsky, 1998; Somers et al., 1995; Nykamp and

Tranchina, 2000; Pugh et al., 2000). However, these theories did not attempt to use a more realistic cortical circuitry. Our model’s lateral connectivity is also very different from models based on Hebbian ideas of activity-driven correlations (see, e.g., Troyer et al., 1998).

The model’s “neurons” are integrate-and-fire (I&F) point neurons and as such represent a considerable simplification of the actual network elements. Even with this simplifying approximation, simulations of such a large-scale model (~16,000 point-neurons) are very time consuming, and parameter studies are difficult. It is even harder to directly analyze the model network mathematically and thereby obtain critical intuition about cortical mechanisms. One purpose of this article is to describe a reduction of our large-scale model network to a simpler, spatially coarse-grained system (CG) for firing rates of neuronal subpopulations (though a detailed derivation will appear elsewhere) (Shelley, McLaughlin, and Cair, 2001). This reduction allows for spatially varying architecture, cortical maps, and input but also explicitly models the effect of having quantities, such as preferred spatial phase or stochastic input conductances (noise), that may vary widely from cortical neuron to cortical neuron (i.e., are disordered). This is very important, for example, in capturing the “phase-averaging” that occurs in producing cortico-cortical conductances in our I&F model and that underlies its simple-cell responses (Wielaard et al., 2001). The CG reduction has the form of a set of nonlinear spatiotemporal integral equations for “phase-averaged” firing rates across the cortex.

Here we use the CG reduction of our model of macaque visual cortex to understand its response to drifting grating stimulation, which is commonly used in experiments to characterize a cortical cell’s orientation selectivity. As one example, under drifting grating stimulation, the I&F model has cortico-cortical conductances that are nearly time invariant (Wielaard et al., 2001). The coarse-grained reduction shows clearly the underlying mechanism for this invariance. The superposition of cortical inputs acts as an average over the preferred spatial phases of the impinging neurons, and if the distribution of preferred spatial phases is taken as being uniform, this phase average converts to a time average—producing time-invariant cortico-cortical input. In this manner, firing rates averaged over the temporal period of the drifting grating become natural objects of study in our CG system. As a second example, simple cells within the I&F model

of McLaughlin et al. (2000) show intriguing spatial patterns of selectivity and firing rate relative to pinwheel centers of hypercolumns: those nearer the centers have higher firing rates and are more selective for orientation than those farther from the centers. We study analytically stripped-down versions of the CG system and show how in a network with strong cortical inhibition these observed patterns of response arise through an interaction of the two-dimensional cortical architecture with the orientation map of the input. Further, we evolve numerically the fully nonlinear CG version of our cortical network and show that it reproduces—at far less computational cost—other salient features of our full I&F network simulations. This suggests that such coarse-grained systems will be useful in larger-scale modeling of cortical response. Finally, we use these simulations to study cortical response to changes in stimulus contrast and the length-scales of synaptic coupling. These studies show, for example, that contrast invariance in orientation selectivity is most pronounced near pinwheel centers and that the smoothing effects of noise can play a crucial role in enhancing contrast invariance. In spite of the success of the CG reduction, one should note that the coarse-grained asymptotics is a large  $N$  limit; hence, it will not capture finite size effects (which one does see in numerical simulations of the I&F system and most certainly in *in vivo* response).

While our coarse-graining approach is focused on understanding a particular model of primary visual cortex, several elements of our theoretical formalism have been described before in different or more idealized settings. For example, others have invoked a separation of time-scales—say, “slow” synapses—to convert conductance-based models of spiking neurons to rate models (e.g., Ermentrout, 1994; Bressloff and Coombes, 2000). Here we invoke a similar separation of time-scales but one associated instead with the observation of large, primary inhibitory, conductances in our model cortex when under stimulation (Wieland et al., 2001; Shelley et al., 2001). Others have also employed coarse-graining arguments to study population responses in networks of spiking neurons (e.g., Gerstner, 1995; Bressloff and Coombes, 2000; Laing and Chow, 2001). Treves (1993) developed a “mean-field” theory, based on population density theory, of the dynamics of neuronal populations that are coupled all-to-all and also outlined some formulational aspects of including disordered network couplings. In our model, a very important source of disorder is that of the preferred spatial phases, which are set by the LGN

input to the cortical cells. Nykamp and Tranchina (2000, 2001) used a population density model (due to Knight et al., 1996) to study the recurrent feedback, point-neuron model of cat visual cortex of Somers et al. (1995), where the cortical architecture was reduced to one-dimensional coupling in orientation. Nearly all of these approaches bear some structural resemblance to the phenomenological mean-field models as originally proposed by Wilson and Cowan (1973) and used, for example, by Ben-Yishai et al. (1995) to study orientation selectivity in a recurrent network with ring architecture. Again, our approach focuses on our detailed I&F model and uses asymptotic arguments to reduce it to a CG description in terms of mean firing rates—a reduction that does not introduce any additional phenomenological parameters into the model.

## 2. Methods

Here we describe briefly those components of our large-scale neuronal network model of layer 4C $\alpha$  that are necessary for understanding its architecture and that are relevant to its CG reduction. A more complete description is found in McLaughlin et al. (2000) and Wieland et al. (2001).

### 2.1. Basic Equations of the Model

The model is comprised of both excitatory and inhibitory I&F point neurons (75% excitatory, 25% inhibitory) whose membrane potentials are driven by conductance changes. Let  $v_P^j$  ( $v_I^j$ ) be the membrane potentials of excitatory (inhibitory) neurons. Each potential evolves by the differential equation

$$\begin{aligned} \frac{dv_P^j}{dt} = & -g_R v_P^j - g_{PE}^j(t)[v_P^j - V_E] \\ & - g_{PI}^j(t)[v_P^j - V_I], \end{aligned} \quad (1)$$

together with voltage reset when  $dv_P^j(t)$  reaches “spiking threshold.” Here  $P = E, I$ , and the superscript  $j = (j_1, j_2)$  indexes the spatial location of the neuron within the two-dimensional cortical layer. We first specified the cellular biophysical parameters, using commonly accepted values: the capacitance  $C = 10^{-6} F \text{ cm}^{-2}$ , the leakage conductance  $g_R = 50 \times 10^{-6} \text{ Omega}^{-1} \text{ cm}^{-2}$ , the leakage reversal potential  $V_R = -70 \text{ mV}$ , the excitatory reversal potential  $V_E = 0 \text{ mV}$ , and the inhibitory reversal potential  $V_I = -80 \text{ mV}$ . We took the spiking threshold as

−55 mV, and the reset potential to be equal to  $V_R$ . The membrane potential and reversal potentials were normalized to set the spiking threshold to unity and the reset potential (and thus  $V_R$ ) to zero, so that  $V_E = 14/3$ ,  $V_I = -2/3$ , and generally  $-2/3 \leq v_E^j, v_I^j \leq 1$ . The capacitance does not appear in Eq. (1) as all conductances were redefined to have units of  $s^{-1}$  by dividing through by  $C$ . This was done to emphasize the time-scales inherent in the conductances. For instance, the leakage time-scale is  $\tau_{leak} = g_R^{-1} = 20$  ms. True conductances are found by multiplication by  $C$ .

## 2.2. Conductances

The time-dependent conductances arise from input forcing (through the LGN), from noise to the layer, and from cortical network activity of the excitatory and inhibitory populations. These excitatory/inhibitory conductances have the form

$$g_{PE}^j(t) = g_{lgn}^j(t) + g_{PE}^0(t) + S_{PE} \sum_k K_{j-k}^{PE} \times \sum_l G_E(t - t_l^k), \quad \text{excitatory}, \quad (2)$$

$$g_{PI}^j(t) = g_{PI}^0(t) + S_{PI} \sum_k K_{j-k}^{PI} \times \sum_l G_I(t - T_l^k), \quad \text{inhibitory}, \quad (3)$$

where  $P = E$  or  $I$ . Here  $t_l^k$  ( $T_l^k$ ) denotes the time of the  $l$ th spike of the  $k$ th excitatory (inhibitory) neuron, defined as  $v_E^j(t_l^k) = 1$  ( $v_I^j(T_l^k) = 1$ ).

The conductances  $g_{PP'}^0(t)$  are stochastic and represent activity from other areas of the brain. Their means and standard deviations were taken as  $g_{EE}^0 = g_{IE}^0 = 6 \pm 6$   $s^{-1}$ ,  $g_{EI}^0 = g_{II}^0 = 85 \pm 35$   $s^{-1}$ . These conductances have an exponentially decaying autocorrelation function with time constant 4 ms. Note that in the model, as currently configured, the inhibitory stochastic conductances are much larger than the excitatory. This imbalance is consistent with a cortex in which cortico-cortical inhibition dominates, producing cells that are selective for orientation and the approximate linearity of simple cells.

The kernels  $K_k^{PP'}$  represent the spatial coupling between neurons. Only local cortical interactions (i.e.,  $< 500$   $\mu\text{m}$ ) are included in the model, and these are assumed to be isotropic (Fitzpatrick et al., 1985; Lund, 1987; Callaway and Wiser, 1996; Callaway, 1998), with

Gaussian profiles:

$$K_j^{PP'} = A_{PP'} \exp(-|jh|^2/L_{PP'}^2), \quad (4)$$

where  $|jh| = |(j_1, j_2)h|$  is a distance across the cortical surface ( $h$  can be considered a distance between neighboring neurons). Based on the same anatomical studies, we estimate that the spatial length-scale of monosynaptic excitation exceeds that of inhibition, with excitatory radii of order  $L_{PE} \sim 200$   $\mu\text{m}$  and inhibitory radii of order  $L_{PI} \sim 100$   $\mu\text{m}$ . These kernels are normalized by choice of  $A_{PP'}$  to have unit spatial sum (i.e.,  $\sum_j K_j^{PP'} = 1$ ).

The cortical temporal kernels  $G_P(t)$  model the time course of synaptic conductance changes in response to arriving spikes from the other neurons. In McLaughlin et al. (2000) and Wielaard et al. (2001), they are taken as generalized  $\alpha$ -functions, with times to peak of 3 ms for excitation and 5 ms for inhibition, and are based on experimental observations (Azouz et al., 1997; Gibson et al., 1999). The kernels are normalized to have unit time integral.

The model's behavior depends on the choice of the cortico-cortical synaptic coupling coefficients:  $S_{EE}, S_{EI}, S_{IE}, S_{II}$ . As all cortical kernels are normalized, these parameters label the strength of interaction. In the numerical experiments reported in McLaughlin et al. (2000) and Wielaard et al. (2001), the strength matrix ( $S_{EE}, S_{EI}, S_{IE}, S_{II}$ ) was set to (0.8, 9.4, 1.5, 9.4). This choice of synaptic strengths made the model stable, with many simple, orientationally selective cells.

## 2.3. LGN Response to Visual Stimuli

For *drifting grating stimuli*, the “screen” has intensity pattern  $I = I(\mathbf{X}, t; \theta, \dots)$  given by

$$I = I_0[1 + \epsilon \sin[\mathbf{k} \cdot \mathbf{X} - \omega t + \psi]], \quad (5)$$

where  $\mathbf{k} = |k|(\cos \theta, \sin \theta)$ . Here  $\theta \in [-\pi, \pi)$  denotes the orientation of the sinusoidal pattern on the screen,  $\psi \in [0, 2\pi)$  denotes its phase,  $\omega \geq 0$  its frequency,  $I_0$  its intensity, and  $\epsilon$  its “contrast.”

As a fairly realistic model for the processing of the visual stimulus along the precortical visual pathway (*Retina*  $\rightarrow$  *LGN*  $\rightarrow$  *V1*), in McLaughlin et al. (2000) and other works the input to a cortical neuron is described by a linear superposition of the output of a collection of model LGN neurons (i.e., convergent input). The firing rate of each LGN cell is itself modeled

as the rectification (since firing rates must be nonnegative) of a linear transformation of the stimulus intensity  $I(\mathbf{X}, t)$ , Eq. (5), where the space/time kernels were chosen in McLaughlin et al. (2000) to agree with experimental measurements in macaque monkey (Benardete and Kaplan, 1999; Shapley and Reid, 1998). These filters have two possible polarities (“on-cells” or “off-cells”) and are arranged spatially into segregated and aligned sets of like polarity (Reid and Alonso, 1995). The placement and symmetries of this spatial arrangement confers, among other things, a preferred angle of orientation  $\theta_j$  and preferred spatial phase  $\phi_j$ , in the LGN input to the  $j$ th cortical neuron.

Here, we replace this detailed model of the input to each cortical cell with a parametrization and note that for sufficiently large contrast ( $\epsilon \geq 0.25$ ) the LGN input is captured approximately by

$$g_{lgn}^j = C\epsilon \left( 1 + \frac{1}{2}(1 + \cos 2(\theta_j - \theta)) \right) \times \sin\left(\frac{2\pi}{\lambda}t - \phi_j\right), \quad (6)$$

where  $\lambda = 2\pi/\omega$  is the temporal period of the stimulus, and  $\phi_j \in [0, 2\pi)$  (with  $C \approx 80$  in McLaughlin et al., 2000). (Note:  $g_{lgn}$  is  $\pi$ -periodic; the direction of grating drift is not captured in this form.) This parametrization can be derived analytically, and its validity has been tested and confirmed numerically (McLaughlin and Kovacic, 2001). This derivation shows that the linear growth of both mean and temporal modulation with contrast  $\epsilon$  in Eq. (6) follows from the onset of strong rectification of the spatial filters. This parametrization captures neither low contrast behavior, where the temporal modulations occur against a fixed background mean, nor models the saturation of individual LGN cells at high contrast. It does capture an important feature of the input from LGN to cortex. Because of the approximate axisymmetry of the receptive field of a single LGN cell, its average firing rate is independent of the orientation of the drifting grating. Hence, the sum of activities of many such cells, averaged over time, is likewise independent of stimulus orientation (Troyer et al., 1998; Sompolinsky and Shapley, 1997), or

$$\langle g_{lgn}(\cdot; \theta) \rangle_t = \bar{g}. \quad (7)$$

That is, the time-averaged LGN input is *independent* of stimulus orientation  $\theta$ , information about which is encoded only in temporal modulations.

Optical imaging of upper layer (2/3) cortical response suggests that the preferred angle is mapped across the cortex in the form of pinwheel patterns that regularly tile the cortical layer (Misc3; Maldonado et al., 1997). Figure 1 shows a 1 mm<sup>2</sup> detail from Blasdel (1992), containing four pinwheel patterns each surrounding a pinwheel center. Optical imaging coupled to electrode measurements suggest further that this structure persists as an orientation hypercolumn down through the cortical layer (Maldonado et al., 1997). The apparently smooth change in orientation preference across the cortical layer, at least away from pinwheel centers, is consistent with recent measurements of DeAngelis et al. (1999) showing that preferred orientation of nearby cortical neurons is strongly correlated.

In McLaughlin et al. (2000), a 1 mm<sup>2</sup> region of  $4C\alpha$  is modeled as a set of four such orientation hypercolumns, each occupying one quadrant (see Fig. 2). Within the  $i$ th hypercolumn,  $\theta_j = a_i \pm \Theta_j/2$ , where  $\Theta$  is the angle of the ray from the pinwheel center. The choice of sign determines the handedness of the pinwheel center. This sign and  $a_i$  are chosen so that the mapping of preferred orientation is smooth across the whole region, except at pinwheel centers (although this continuity does not seem to be strictly demanded by optical imaging data) (Blasdel, 1992; Bonhoeffer and Grinvald, 1991). Thus, within a hypercolumn, the angular coordinate  $\Theta$  essentially labels the preferred orientation of the LGN input.

The experiments of DeAngelis et al. (1999) show that, unlike preferred orientation, the preferred spatial phase  $\phi$  of each cortical cell is not mapped in a regular fashion. Indeed, their work suggest that  $\phi_j$  is distributed randomly from neuron to neuron, with a broad distribution. We assume that this broad distribution is uniform.

### 3. Results

While amenable to large-scale simulation, the full-network equations of the I&F point neuron model (Eq. (1)) are typically too complex to study analytically. We use instead an asymptotic reduction of the full network to a spatially coarse-grained network, expressed in terms of average firing rates over coarse-grained cells (termed a *CG-cell*). This reduced description is more amenable to analytical investigation and easier to study numerically. The asymptotic methods that produce the coarse-grained system include multiple time-scale analysis, “Monte-Carlo” approximation

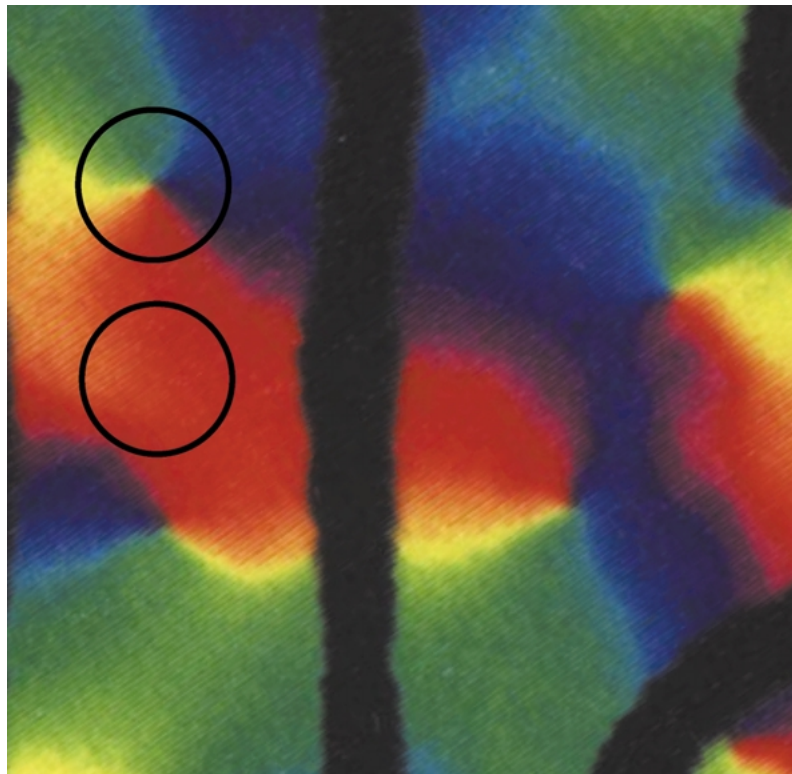


*Figure 1.* From Blasdel (1992) (with author's permission), a detail from an optical imaging of the orientation mapping across the superficial layers of macaque V1, over an area  $\sim 1 \text{ mm}^2$ . The image shows four orientation hypercolumns with pinwheel centers. The superimposed circles show the estimated length-scale of monosynaptic inhibition in the local connections of layer  $4C\alpha$ .

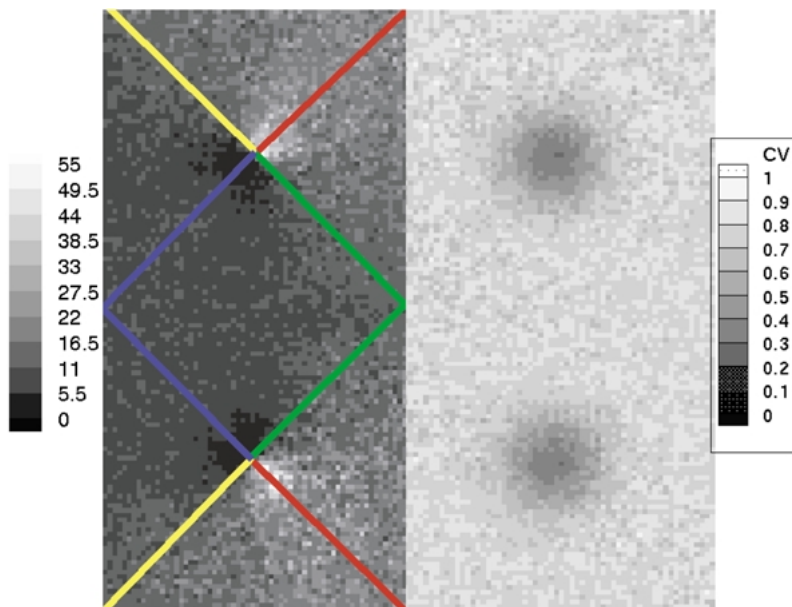


*Figure 2.* From the point-neuron network simulations of McLaughlin et al. (2000), the spatial distribution of time-averaged firing-rates (left panel) and of circular variance (right panel) across the model cortical surface ( $\sim 1 \text{ mm}^2$ ).

by integrals of the summations in the conductances (Eq. (3)), such as

$$\tilde{g}_{EE} = S_{EE} \sum_{k,l} K_{j-k}^{EE} G_E(t - t_l^k),$$

and a probabilistic closure over subpopulations.

Another part of this reduction involves consideration of dynamical time-scales in cortical response. There are three important time-scales in Eq. (1): the time-scale of the stimulus modulation,  $\tau_{lgn} = O(10^2)$  ms; a shorter time scale of the cortical-cortical interaction times (and the noise, presumably synaptically mediated),  $\tau_s = O(4)$  ms (Azouz et al., 1997; Gibson et al., 1999); and the shortest, the response time of neurons within an active network,  $\tau_g = O(2)$  ms (Wieland et al., 2001; Shelley et al., 2001). We emphasize that the latter is a property of network activity. While the separation of  $\tau_s$  and  $\tau_g$  is only a factor of two, we have found that this is sufficient to cause cortical neurons to respond with near instantaneity to presynaptic cortical input (Shelley et al., 2001). In our reduction analysis, we assume and use this separation of time scales,

$$\frac{\tau_g}{\tau_s}, \frac{\tau_g}{\tau_{lgn}} \ll 1,$$

to help relate conductances to firing rates.

While the technical details of this reduction are lengthy and will appear elsewhere (Shelley, McLaughlin, and Cai, 2001), we outline some of the critical steps in the coming section.

### 3.1. A Coarse-Grained Network

Cortical maps such as orientation preference, spatial frequency preference, and retinotopy are arranged in regular patterns across the cortex. Thus, we partition the two-dimensional cortical layer into CG-cells, each of which is large enough to contain many neurons and yet small enough that these mapped properties are roughly the same for each neuron in the CG-cell. These mapped properties are then treated as constants across each CG-cell. This is in opposition to quantities such as preferred spatial phase  $\phi$ , which seem to be distributed randomly from cortical neuron to cortical neuron. Accordingly, we also assume that within each CG-cell there are sufficiently many neurons that the distributions of disordered quantities, such as preferred spatial phase, are well sampled.

**3.1.1. The Preferred Spatial Phase.** We first give the result for the case of only one disordered quantity—the preferred spatial phase—and then indicate how the results are modified if there are other disordered fields, such as the random input conductances. Before introducing the spatially coarse-grained tiling, we partition the  $N^E$  excitatory ( $N^I$  inhibitory) neurons in the layer into subsets with like spatial phase preference. Divide the interval  $[0, 2\pi)$  of preferred spatial phases into  $P$  equal subintervals of width  $\Delta\phi = 2\pi/P$ :

$$\Phi_p \equiv [(p-1)\Delta\phi, p\Delta\phi), \quad p = 1, \dots, P,$$

and partition the set of  $N^E$  excitatory neurons as

$$\mathcal{S}^{E,p} \equiv \{\text{all excitatory neurons with } \phi \in \Phi_p\},$$

for  $p = 1, \dots, P$ .

If  $N^{E,p}$  is the number of neurons in  $\mathcal{S}^{E,p}$ , then  $N^E = \sum_{p=1}^P N^{E,p}$ . The inhibitory neurons are partitioned similarly, with like notation ( $N^I, N^{I,p}, \mathcal{S}^{I,p}$ ).

With this partitioning of spatial phase preference, a typical cortico-cortical conductance takes the form

$$\begin{aligned} \tilde{g}_{EE}^j(t) &\equiv S_{EE} \sum_{k=1}^{N^E} \sum_l K_{j-k}^{EE} G_E(t - t_l^k) \\ &= S_{EE} \sum_{p=1}^P \sum_{k_p \in \mathcal{S}^{E,p}} \sum_l K_{j-k_p}^{EE} G_E(t - t_l^{k_p}), \end{aligned} \quad (8)$$

where the sum over  $l$  is taken over all spikes of the  $k_p$ th neuron, and the subsequence  $\{k_p\}$  runs over the  $N^{E,p}$  neurons in  $\mathcal{S}^{E,p}$ .

Next, let  $\{\mathcal{N}_\kappa, \kappa = (\kappa_1, \kappa_2) \in Z^2\}$  denote the partitioning of the cortical layer into coarse-grained spatial cells (CG-cells), (see Fig. 3)—with the  $\kappa$ th CG-cell containing  $N_\kappa = N_\kappa^E + N_\kappa^I$  excitatory and inhibitory neurons, of which  $N_\kappa^p = N_\kappa^{E,p} + N_\kappa^{I,p}$  have preferred spatial phase  $\phi \in \Phi^p$ . Clearly,

$$N_\kappa^E = \sum_{p=1}^P N_\kappa^{E,p} \quad \text{and} \quad N_\kappa^I = \sum_{p=1}^P N_\kappa^{I,p}.$$

Thus, each excitatory neuron in the  $\kappa$ th CG-cell with preferred spatial phase  $\phi \in \Phi^p$  is labeled by the (vector) sum  $k_p = \kappa + k'_p, k'_p \in \mathcal{S}_\kappa^{E,p}$ , those excitatory neurons in the  $\kappa$ th CG-cell with preferred spatial phase in  $\Phi^p$ .

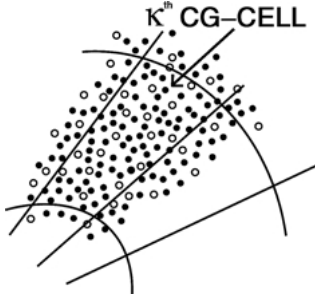


Figure 3. A schematic illustrating the tiling of the cortical surface into coarse-grained cells and in particular the representative  $\kappa$ th CG-cell. The circles represent excitatory model neurons, with the open circles representing those model neurons whose preferred spatial phase sits in a single phase bin—say,  $S_1^E$ .

Returning to Eq. (8), then

$$\begin{aligned} \tilde{g}_{EE}^j(t) &= S_{EE} \sum_{p=1}^P \sum_{\kappa, l} \sum_{k'_p \in \mathcal{S}_{\kappa}^{E,p}} K_{j-(\kappa+k'_p)}^{EE} \\ &\quad \times G_E(t - t_l^{\kappa+k'_p}). \end{aligned} \quad (9)$$

We assume now that the spatial interaction kernels are nearly constant over each CG-cell—i.e.,

$$K_{j-(\kappa+k'_p)}^{EE} \simeq K_{j-\kappa}^{EE}, \quad (10)$$

—and that the spike times  $t_l^k$  are of the form

$$t_l^{\kappa+k'_p} \simeq \tau_{\kappa}^p(t) \cdot l + \psi_{\kappa+k'_p}, \quad (11)$$

where  $\tau_{\kappa}^p(t)$  is the (slowly varying) mean interspike time for the (excitatory) neurons in the  $\kappa$ th CG-cell with preferred spatial phase  $\phi \in \Phi^p$ . Here it is assumed that the phases  $\psi_{\kappa+k'_p}$  statistically cover the interval  $[t_l^{\kappa}, t_{l+1}^{\kappa}]$  uniformly, as  $k'_p$  runs over  $\mathcal{S}_{\kappa}^{E,p}$ . Thus, the sum over  $k'_p$  (the excitatory neurons in the  $\kappa$ th CG-cell) reduces to a temporal phase average that can be evaluated with Monte-Carlo integration (Feller, 1968):

$$\frac{1}{N} \sum_{i=1}^N f(t_i) \simeq \frac{1}{L} \int_0^L f(t) dt \pm \sqrt{\frac{\langle f^2 \rangle - \langle f \rangle^2}{N}}, \quad (12)$$

where  $\{t_i; i = 1, 2, \dots, N\}$  denotes  $N$  points, chosen independently from a uniform distribution over the interval  $[0, L]$ , and

$$\langle F \rangle \equiv \frac{1}{N} \sum_{i=1}^N F(x_i).$$

In this manner, Monte Carlo integration shows that the sample cortico-cortical conductance  $\tilde{g}_{EE}(t)$  is approximated by

$$\begin{aligned} \tilde{g}_{EE}^j(t) &\simeq S_{EE} \sum_{p=1}^P \sum_{\kappa, l} N_{\kappa}^{E,p} K_{j-\kappa}^{EE} \\ &\quad \times \int_{t_l^{\kappa}}^{t_{l+1}^{\kappa}} G_E(t-s) \frac{1}{\tau_{\kappa}^p(s)} ds \\ &\simeq S_{EE} \sum_{\kappa, l} K_{j-\kappa}^{EE} \\ &\quad \times \int_{t_l^{\kappa}}^{t_{l+1}^{\kappa}} G_E(t-s) \left[ \sum_{p=1}^P N_{p,\kappa}^E \frac{1}{\tau_{\kappa}^p(s)} \right] ds \\ &\simeq S_{EE} \sum_{\kappa, l} N_{\kappa}^E K_{j-\kappa}^{EE} \\ &\quad \times \int_{t_l^{\kappa}}^{t_{l+1}^{\kappa}} G_E(t-s) \langle m_{\kappa} \rangle_{\phi}(s) ds \\ &\simeq S_{EE} \sum_{\kappa} N_{\kappa}^E K_{j-\kappa}^{EE} \\ &\quad \times \int_{-\infty}^t G_E(t-s) \langle m_{\kappa} \rangle_{\phi}(s) ds, \end{aligned} \quad (13)$$

where

$$m_{\kappa}(\phi) = \frac{1}{\tau_{\kappa}^p}, \quad \text{for } \phi \in \Phi^p$$

$$\langle m_{\kappa} \rangle_{\phi} \equiv \int m_{\kappa}(\phi) \rho(\phi) d\phi \simeq \frac{1}{N_{\kappa}^E} \sum_{p=1}^P N_{\kappa}^{E,p} \frac{1}{\tau_{\kappa}^p(s)},$$

and  $\rho(\phi)$  is the probability density associated with  $\phi$ . Finally, for convenience we adopt a continuum notation and define

$$\begin{aligned} \tilde{g}_{EE}(\mathbf{x}, t) &= \mathbf{K}_{EE}[\langle m \rangle_{\phi}](\mathbf{x}, t) \\ &\equiv S_{EE} K_{EE} * G_E * \langle m \rangle_{\phi}(\mathbf{x}, t) \\ &\equiv S_{EE} \int d^2 \mathbf{x}' \int_{-\infty}^t ds K_{EE}(\mathbf{x} - \mathbf{x}') \\ &\quad \times G_E(t-s) \langle m \rangle_{\phi}(\mathbf{x}', s), \end{aligned} \quad (14)$$

where  $\mathbf{x}$  denotes the spatial location of the  $\kappa$ th CG-cell within the cortical layer.

Inserting expressions such as Eq. (14) into Eq. (1) and rearranging them yield a voltage equation of the form

$$\frac{dv_P^j}{dt} = -g_T^j [v_P^j - V_S^j]. \quad (15)$$



Here the total conductance  $g_T$  and the “effective reversal potential”  $V_s$  are expressions in terms of coarse-grained conductances; hence, they depend explicitly on the firing rates  $m_P(\mathbf{x}, t)$  rather than on the firing times. We refer to the next step in the derivation of a closed system of equations for these firing rates alone as the “closure step”—a step that eliminates the voltage  $v_P^j$ , leaving only equations in terms of  $m_P(\mathbf{x}, t)$ .

This step begins with the observations that under high-contrast visual stimulation, the total conductance increases substantially (Borg-Graham et al., 1998; Hirsch et al., 1998; Anderson et al., 2000). Thus, the relaxation time-scale  $[g_T]^{-1}$  can be very short if the total conductance is sufficiently high. That is, cortical activity can create an emergent time-scale that is even shorter than synaptic time-scales (Wielaard et al., 2001; Shelley et al., 2001). Under the assumption that this relaxation time-scale is short enough that it is well-separated from the longer synaptic time-scales over which  $g_T$  and  $V_s$  vary, Eq. (15) can be integrated between successive spikes with  $g_T$  and  $V_s$  held constant. This is because the time between spikes (for  $V_s > 1$ ) likewise scales with the rapid relaxation time. This integration yields a logarithmic expression for the average interspike interval, whose inverse is the firing rate  $m_P(\mathbf{x}, t)$ .

In this manner, with asymptotic techniques (including multiple time-scale analysis, Monte Carlo approximation, and a probabilistic closure), the full network of I&F neurons can be reduced to coarse-grained equations for the average excitatory and inhibitory firing rates of neurons in the CG-cell at  $\mathbf{x}$ :

$$m_P(\mathbf{x}, t; \phi) = \mathcal{N}(g_{lgn}(\mathbf{x}, t; \phi), \tilde{g}_{PP'}(\mathbf{x}, t)) \quad (16)$$

for  $P = E$  and  $I$ , and where the free index  $P'$  denotes dependence of the RHS on both  $P' = E$  and  $I$ . Here,

$$\mathcal{N} = \frac{-g_T(\mathbf{x}, t)}{\log\left(\frac{\{I_D(\mathbf{x}, t) - g_T(\mathbf{x}, t)\}^+}{g_T(\mathbf{x}, t) + \{I_D(\mathbf{x}, t) - g_T(\mathbf{x}, t)\}^+}\right)}, \quad (17)$$

where

$$g_{T,P}(\mathbf{x}, t) \equiv g_R + g_{lgn}(\mathbf{x}, t) + \sum_{P'} (\tilde{g}_{PP'}(\mathbf{x}, t) + \bar{f}_{P'}) \quad (18)$$

is the total conductance, and

$$I_{D,P}(\mathbf{x}, t) \equiv V_E g_{lgn}(\mathbf{x}, t) + \sum_{P'} V_{P'} (\tilde{g}_{PP'}(\mathbf{x}, t) + \bar{f}_{P'}) \quad (19)$$

is the so-called difference current (Wielaard et al., 2001), as it arises as the difference of excitatory and inhibitory synaptic currents.

Several points are worth noting:

- The thresholding in Eq. (17) is taken to imply that  $\mathcal{N} = 0$  if  $I_D(\mathbf{x}, t) - g_T(\mathbf{x}, t) \leq 0$ . This latter quantity is the *threshold membrane current*, obtained by setting  $v^j = 1$  in Eq. (1), and its positivity is a necessary condition for cell spiking. (In dimensional units, the threshold current would be  $I_D(\mathbf{x}, t) - \bar{V} g_T(\mathbf{x}, t)$ , where  $\bar{V}$  is the spiking threshold.) Note that for positive threshold current,  $\mathcal{N} = -g_T / \log[1 - g_T / I_D]$ .
- As we considered the preferred phase  $\phi$  as the only disordered quantity across a CG-cell, we have included in the above only the means,  $\bar{f}_{P'}$ , but not the noisy fluctuations of the stochastic input conductances.
- The quantity  $V_s = I_D / g_T$ , a ratio of weighted synaptic conductances, is an effective reversal potential that, under the separation of time-scales assumption of this analysis, closely approximates the intracellular potential of a cell when subthreshold or blocked from spiking.
- It can be shown that  $\mathcal{N}$  increases (decreases) monotonically with increasing excitatory (inhibitory) conductance.

### 3.1.2. Including Another Disordered Quantity.

Thus far we considered only the phase  $\phi_j$  as being disordered. Now assume that, in addition, the stochastic conductance contributions are stationary processes that are independent and identically distributed from cortical neuron to cortical neuron and that their temporal fluctuations do not break the separation of time-scales constraint (this is valid because these fluctuations are on the synaptic time-scales). These fluctuations can then be averaged over a CG-cell in a manner essentially identical as that for the preferred spatial phase. Write these conductances as

$$f_{PP'}^j(t) = \bar{f}_{P'} + \eta_{P'}^j(t),$$

where  $\bar{f}_P$  denotes the mean and  $\eta_P$  the random fluctuations (of expectation zero), with density  $\mathcal{F}_P(\eta) d\eta$ . Averaging over the many neuronal contributions within a CG-cell then samples the distribution of  $\eta_E$  and  $\eta_I$ . Equation (16) becomes generalized as an equation for a CG-cell firing rate  $n_P(\mathbf{x}, t; \phi, \eta_E, \eta_I)$ , with  $\langle m_{P'} \rangle_\phi$  replaced by  $\langle n_{P'} \rangle_{\phi, \eta_E, \eta_I}$  (as with the phase with density  $\rho$ , averages are defined with respect to the densities  $\mathcal{F}_P$ ),

and with  $\bar{f}_{P'}$  replaced by  $\bar{f}_{P'} + \eta_{P'}$  in Eqs. (18) and (19) for  $g_T$  and  $I_D$ , respectively. As we are interested here only in the “noise-averaged” quantities, we define

$$m_P(\mathbf{x}, t; \phi) = \langle n_P \rangle_{\eta_E, \eta_I}.$$

The equation for  $m_P(\mathbf{x}, t; \phi)$  is again Eq. (16), but with  $\mathcal{N}$  redefined as

$$\mathcal{N} \equiv \int_{I_D > g_T} \frac{-g_T}{\log[1 - g_T/I_D]} \mathcal{F}_E(\eta_E) \mathcal{F}_I(\eta_I) d\eta_E d\eta_I. \quad (20)$$

It is important to note that describing the densities  $\mathcal{F}_P$  is generally nontrivial. If the “noise” is being generated by, say, a synaptically mediated, Poisson-spiking process, then these densities will be highly dependent on the form of the postsynaptic conductance course,  $G_P$ . Only in the high-rate limit can  $\mathcal{F}_P$  be described easily through a version of the *central limit theorem*. And even in that case, finding  $m_P(\mathbf{x}, t; \phi)$  requires the evaluation of two-dimensional integrals, which while numerically tractable, is expensive. In the case where the densities  $\mathcal{F}_P$  are uniform, the two-dimensional integrals in Eq. (20) can be analytically reduced to one-dimensional integrals through an explicit integration, thus considerably ameliorating the cost.

**3.1.3. Averaging Closes the CG Equations.** It is an important mathematical property of this reduced, coarse-grained system that the coarse-grained equations (16) can be averaged with respect to  $\phi$  to yield closed space- and time-dependent equations for the phase-averaged firing rates:

$$\langle m_P \rangle_\phi(\mathbf{x}, t) = \langle \mathcal{N}(g_{lgn}(\mathbf{x}, t; \phi), \tilde{g}_{PP'}(\mathbf{x}, t)) \rangle_\phi. \quad (21)$$

Thus, these systems can be solved for phase-averaged quantities directly through Eq. (21) and then by reconstructing phase-dependent quantities through Eq. (16). Here we have not been specific about the spatial phase dependence of  $g_{lgn}$ . For drifting gratings, as suggested earlier, it will be modeled by a temporal phase shift but more generally will depend strongly on the stimulus class; the phase dependence of  $g_{lgn}$  for contrast reversal stimuli is considerably different and more complicated (see Wielaard et al., 2001, Fig. 2) than for drifting gratings and poses a rigorous test for simple cell response.

Equations (16) and (21) are the main results of this section. They constitute coarse-grained integral equations for the local firing rates  $m_E(\mathbf{x}, t)$  and  $m_I(\mathbf{x}, t)$ .

These coarse-grained results can be seen as the limit of a population density formulation, under the separation of time-scales induced by the model visual cortex being in a high-conductance state (Shelley, McLaughlin, and Cai, 2001). While these coarse-grained equations are also similar to mean-field models for firing rates, differences and distinctions include (1) their derivation from the full I&F network, without the introduction of phenomenological parameters; (2) the use of a high-conductance cortical state to achieve a temporal scale separation; and (3) the simultaneous presence of ordered spatial maps (such as for orientation preference) and disordered spatial maps (such as for spatial phase preference).

This CG reduction is quite specific to capturing key elements of our large-scale model of an input layer of visual cortex. The CG equations (16) retain dependence on spatial location within the two-dimensional cortical layer through their dependence on the cortical coordinate  $\mathbf{x}$ , and interactions are relative to cortical location. This is far from “all-to-all.” The form of the input reflects our understanding of the processing of visual information in the precortical pathway. An important structural trait is that cortico-cortical interaction terms depend only on the *spatial phase-averaged* firing rates  $\langle m_P \rangle_\phi$ . This is essential to the analysis that follows. Again, this average arises because the CG-cells contain neurons with measured properties (such as orientation preference) that are well ordered and others (such as spatial phase) that are disordered. Within each CG-cell, we average over the disordered properties.

**3.1.4. Special Cases of the CG Equations.** Equations (16) and (21) are the general form of the CG equations, with nonlinearity given by Eq. (17) or Eq. (20). We find it useful to consider various simplifications, or models, or these equations:

**1. The thresholded-linear model** Here,  $\mathcal{N}_P$  in Eq. (17) is replaced by

$$\mathcal{N} = \{I_D(\mathbf{x}, t; \phi) - g_T(\mathbf{x}, t; \phi)\}^+, \quad (22)$$

where

$$\begin{aligned} I_{D,P} - g_{T,P} &= f(\mathbf{x}, t; \phi) \\ &+ C_{PE} \cdot K_{PE} * G_E * \langle m_E \rangle_\phi(\mathbf{x}, t) \\ &- C_{PI} \cdot K_{PI} * G_I * \langle m_I \rangle_\phi(\mathbf{x}, t), \end{aligned}$$

and

$$\begin{aligned} f(\mathbf{x}, t; \phi) &\equiv -g_R + (V_E - 1) g_{lgn}(\mathbf{x}, t; \phi) \\ C_{PE} &\equiv (V_E - 1) S_{PE} \geq 0 \\ C_{PI} &\equiv (1 - V_I) S_{PI} \geq 0. \end{aligned}$$

This is a useful model, even though it is not an analytical reduction of the full CG equations. First, it captures the nonlinearity of thresholding, while replacing the nonlinear argument with a linear one—the threshold membrane current. Second, it retains monotonic dependencies on excitatory and inhibitory conductances. And third, it retains the proper requirement for threshold to firing, a positive threshold membrane current,  $I_b > g_r$ . Equation (22) is very similar to the Wilson-Cowan mean-field models (Wilson and Cowan, 1973), though with the inclusion, again, of phase-averaged arguments.

**2. The far-field reduction** Consider a single orientation hypercolumn filling the entire plane. Then far from a pinwheel center,  $g_{lgn}$  (at a given phase) will change very little over a coupling length-scale  $L_{PP'}$ , encoded in  $K_{PP'}$  (this statement is especially relevant to the inhibitory length-scales  $L_{PI}$ ; see Fig. 1). In this case, one can seek solutions  $\langle m_P \rangle_\phi$  that likewise vary slowly over these length-scales, in which case

$$\begin{aligned} \tilde{g}_{PP'}(\mathbf{x}, t) &\approx S_{PP'} G_P * \langle m_{P'} \rangle_\phi(\mathbf{x}, t) \\ &= S_{PP'} \int_{-\infty}^t ds G_P(t-s) \langle m_{P'} \rangle_\phi(\mathbf{x}, s), \end{aligned} \quad (23)$$

where only the temporal convolution remains. (This uses that  $K_{PP'}$  has unit spatial integral.) Then Eq. (21), for example, will take the form of *spatially local* fixed point equations,

$$\begin{aligned} \langle m_P \rangle_\phi(\mathbf{x}, t) &= \langle \mathcal{N}(g_{lgn}(\mathbf{x}, t; \phi), \\ &S_{PP'} G_P * \langle m_{P'} \rangle_\phi(\mathbf{x}, t)) \rangle_\phi, \end{aligned} \quad (24)$$

to be solved point-wise in  $\mathbf{x}$ . Note that if  $g_{lgn} = g_{lgn}(\Theta, t; \phi)$  (i.e., as with drifting grating stimuli),  $g_{lgn}$  depends spatially only on the hypercolumn angular coordinate, then the solutions  $\langle m_P \rangle_\phi$  will also depend spatially only on  $\Theta$ .

**3. The near-field model** In the neighborhood of a pinwheel center, the synaptic sampling of cortical cells residing at all angles around the pinwheel center is part of the special character of response there. Accordingly, we model responses in that neighborhood by retaining

only the angular part of the spatial convolution and seeking solutions of the equations:

$$\begin{aligned} \langle m_P \rangle_\phi(\Theta, t) &= \langle \mathcal{N}(g_{lgn}(\Theta, t; \phi), \\ &S_{PP'} G_{P'} * \langle m_{P'} \rangle_\phi(\Theta, t)) \rangle_\phi. \end{aligned} \quad (25)$$

Here, we have assumed that  $g_{lgn}$  depends spatially only on  $\Theta$ , as would be the case for drifting grating stimuli. Obviously, this expression can be averaged once more with respect to  $\Theta$  to yield a closed equation for  $\langle m_P \rangle_\phi$ . This model is very similar to one studied by Ben-Yishai et al. (1995), which they termed the “Hubel-Wiesel model with uniform cortical inhibition.”

The far- and near-field models are very useful for exploring differences in firing-rate patterns near and far from the pinwheel center.

### 3.2. The Special Case of Drifting Grating Stimuli

Visual stimulation by drifting spatial gratings is frequently used experimentally to characterize the orientation selectivity of cortical neurons. The measured neuronal response is typically the neuron’s time-averaged firing rate:

$$\langle m \rangle_t(\theta) = \frac{\text{Number of spikes in time } T}{T},$$

where  $T$  encompasses many cycles of the drifting grating, and  $\theta$  is the orientation of the grating. The dependence of  $\langle m \rangle_t$  on  $\theta$  characterizes the neuron’s selectivity for orientation.  $\langle m \rangle_t$  is a very natural object to study within our coarse-grained equations.

The stimulus has temporal period  $\lambda = 2\pi/\omega$ , and the model cortical network is driven by LGN stimulation (given in Eq. (6)) at the same period, which we denote as

$$g_{lgn}(\mathbf{x}, t; \theta, \phi) = g_{lgn}\left(\Theta(\mathbf{x}), t - \frac{\lambda}{2\pi}\phi; \theta\right), \quad (26)$$

where the dependence on spatial wavenumber  $k$ , intensity  $I_0$ , and contrast  $\epsilon$  have been suppressed in the notation.

We seek solutions  $m_{E,I}$  to the coarse-grained Eq. (16) that reflect the structure of the LGN forcing—that is, are temporally periodic—and shifted relative to the preferred phase  $\phi$ :

$$m_P(\mathbf{x}, t; \theta, \phi) = \bar{m}_P\left(\mathbf{x}, t - \frac{\lambda}{2\pi}\phi; \theta\right), \quad P = E, I. \quad (27)$$

We now restrict our attention to a *uniform phase distribution* on  $[0, 2\pi)$ ,  $\rho = 1/2\pi$ , in which case phase averages become temporal averages—that is,  $\langle \bar{m}_P \rangle_\phi = \langle \bar{m}_P \rangle_t$ . This temporal average is over  $\lambda$ , the period of  $\bar{m}$ , and given that periodicity is equivalent to a long-time average. Further,

$$\begin{aligned} & \int_{-\infty}^t ds G_P(t-s) \langle \bar{m}_P \rangle_\phi(\mathbf{x}, s) \\ &= \int_{-\infty}^t ds G_P(t-s) \langle \bar{m}_P \rangle_t(\mathbf{x}) = \langle \bar{m}_P \rangle_t(\mathbf{x}). \end{aligned}$$

The cortico-cortical conductances then take the form

$$S_{PE} K_{PE} * \langle \bar{m}_E \rangle_t \quad \text{and} \quad S_{PI} K_{PI} * \langle \bar{m}_I \rangle_t \quad (28)$$

and are thus *independent of time* and are only spatial convolutions. This is an important result that reflects fundamentally the architecture of the model and is an approximate feature of our I&F simulations (see Wielaard et al., 2001, Fig. 7).

The coarse-grained Eq. (6) now take the simplified form

$$\begin{aligned} \bar{m}_P \left( \mathbf{x}, t - \frac{\lambda}{2\pi} \phi; \theta \right) &= \mathcal{N} \left( g_{lgn} \left( \Theta(\mathbf{x}), t - \frac{\lambda}{2\pi} \phi; \theta \right), \right. \\ & \left. S_{PP'} K_{PP'} * \langle \bar{m}_{P'} \rangle_t(\mathbf{x}) \right), \quad (29) \end{aligned}$$

for  $P = E, I$ . As the only time and phase dependence is through their difference, the phase average of Eq. (29) again converts to a time average, yielding two closed fixed-point equations for the time-averaged firing rates:

$$\begin{aligned} \langle \bar{m}_P \rangle_t(\mathbf{x}) &= \langle \mathcal{N}(g_{lgn}(\Theta(\mathbf{x}), t; \theta), \\ & S_{PP'} K_{PP'} * \langle \bar{m}_{P'} \rangle_t(\mathbf{x})) \rangle_t, \quad (30) \end{aligned}$$

for  $P = E, I$ . Equation (20) is a beautifully simplified and closed pair of fixed-point equations for the temporally averaged firing rates. Solution of these time-independent equations allows for the reconstruction of time-dependent firing rates from Eq. (29). These expressions are the basis for our analytical and numerical studies, in subsequent sections, on the character of our model's firing-rate patterns and selectivity.

Though we do not directly investigate it here, the linear stability problem associated with these special solutions is relatively tractable since  $\langle \bar{m}_P \rangle_t(\mathbf{x})$  can be considered as the base state, which is time and phase independent. Let  $m_P = \bar{m}_P + \epsilon \tilde{m}$ , where  $\epsilon \ll 1$ .

We assume that the linearized problem is well set—i.e., that there exist unique functions  $\delta \mathcal{N} / \delta \tilde{g}_{PP'}$  such that

$$\begin{aligned} & \mathcal{N}(g_{lgn}, \mathbf{K}_{PE}[\langle m_E \rangle_\phi], \mathbf{K}_{PI}[\langle m_I \rangle_\phi]) \\ &= \mathcal{N}(g_{lgn}, S_{PE} K_{PE} * \langle \bar{m}_E \rangle_t, S_{PI} K_{PI} * \langle \bar{m}_I \rangle_t) \\ &+ \epsilon \sum_{P'=E,I} \frac{\delta \mathcal{N}}{\delta \tilde{g}_{PP'}}(g_{lgn}, S_{PE} K_{PE} * \langle \bar{m}_E \rangle_t, \\ & S_{PI} K_{PI} * \langle \bar{m}_I \rangle_t) \cdot \mathbf{K}_{PP'}[\langle \tilde{m}_{P'} \rangle_\phi] + o(\epsilon), \end{aligned}$$

where  $\mathbf{K}_{PP'}$  is the space-time convolution defined in Eq. (14). Note that the only phase dependence in this expansion is through the LGN forcing:  $g_{lgn} = g_{lgn}(\Theta(\mathbf{x}), t - \frac{\lambda}{2\pi} \phi; \theta)$ . Thus, phase-averaging of this expansion yields

$$\begin{aligned} \langle \bar{m}_P \rangle_t + \epsilon \sum_{P'=E,I} \left\langle \frac{\delta \mathcal{N}}{\delta \tilde{g}_{PP'}} \right\rangle_t(\mathbf{x}) \\ \cdot \mathbf{K}_{PP'}[\langle \tilde{m}_{P'} \rangle_\phi](\mathbf{x}, t) + o(\epsilon). \quad (31) \end{aligned}$$

Finally, substituting this expansion in Eq. (21) and dropping the  $o(\epsilon)$  error term yields the linearized evolution for  $\tilde{m}$ :

$$\langle \tilde{m}_P \rangle_\phi(\mathbf{x}, t) = \sum_{P'=E,I} \left\langle \frac{\delta \mathcal{N}}{\delta \tilde{g}_{PP'}} \right\rangle_t(\mathbf{x}) \cdot \mathbf{K}_{PP'}[\langle \tilde{m}_{P'} \rangle_\phi](\mathbf{x}, t). \quad (32)$$

Rather surprisingly, Eq. (32) is a constant coefficient in time problem for the perturbation  $\langle \tilde{m} \rangle_\phi$ , and is in principle solvable by separation of variables techniques. This simplicity arises because of the phase averaging nature of our network.

The simplicity of these equations in the drifting grating case results from the replacement of phase averages with time averages. This replacement is exact when the distribution of preferred spatial phase uniformly covers  $[0, 2\pi)$ . As measured experimentally in DeAngelis et al. (1999), this phase distribution is broad, indicating that it is a reasonable approximation to assume a uniform phase distribution.

### 3.2.1. Understanding Spatial Patterns of Firing and Selectivity.

A striking feature of our large-scale simulations of the model cortex is the distinctive spatial distributions of firing rates and orientation selectivity, relative to the orientation pinwheel center locations. Figure 2 shows the firing rates and orientation

selectivity across a region containing four orientation hypercolumns (from McLaughlin et al., 2000). Here, orientation selectivity is measured by the *circular variance* of the tuning curves, defined as

$$CV[\langle m \rangle_t(\mathbf{x})] \equiv 1 - \left| \frac{\hat{m}_2(\mathbf{x})}{\hat{m}_0(\mathbf{x})} \right|,$$

where  $\hat{m}_k(\mathbf{x})$  denotes the  $k$ th Fourier coefficient with respect to the stimulus orientation  $\theta$ —i.e.,

$$\hat{m}_k(\mathbf{x}) \equiv \frac{1}{2\pi} \int_0^{2\pi} e^{ik\theta} \langle m \rangle_t(\mathbf{x}; \theta) d\theta.$$

By construction,  $0 \leq CV \leq 1$ . If a cell shows little selectivity in  $\theta$  (that is, the tuning curve is nearly flat in  $\theta$ ), then its CV will be nearly one. Conversely, if the cell is sharply selective, with its tuning curve close to a  $\delta$ -function centered at the cell's preferred angle, then its CV will be close to zero. More generally, CV measures the amplitude of modulation, as measured by  $\hat{m}_1$ , relative to its mean. Increasing this amplitude of modulation typically decreases the circular variance.

Figure 2 shows  $\langle m \rangle_t$  and  $CV[\langle m \rangle_t]$  across the model cortex for the I&F network of simple cells considered by McLaughlin et al. (2000). It shows that the highest firing rates occur near the pinwheel centers, along the maximally excited orientation column, and that (with identically tuned input across the cortex) the sharpest orientation tuning (as measured by low CVs) occurs near the pinwheel centers. Both of these properties result from cortico-cortical interactions, as they are not present in the geniculate input to the layer. The emphasis of our analysis will be on networks whose cortico-cortical conductances are dominated by inhibition, which is the operating regime of the network considered in McLaughlin et al. (2000) and Wiesel et al. (2001). As we will show, the coarse-grained Eq. (30) unveils the mechanisms that underlie these distinct spatial distributions.

We model the cortical layer as a single-orientation hypercolumn that fills the plane, with its pinwheel center at the origin. This is reasonable for the case at hand as the length-scale of monosynaptic inhibition,  $L_{PI}$ , lies below a hypercolumn width, as Fig. 1 well illustrates. In this case of a single hypercolumn, let the stimulus angle  $\theta = 0$  coincide with the coordinate angle  $\Theta = 0$ . Then the angular coordinate  $\Theta$  and the stimulus angle  $\theta$  can be interchanged in interpretation by noting that  $m_P(\Theta, t; \theta) = m_P(2\theta, t; \Theta/2)$ . Accordingly, we

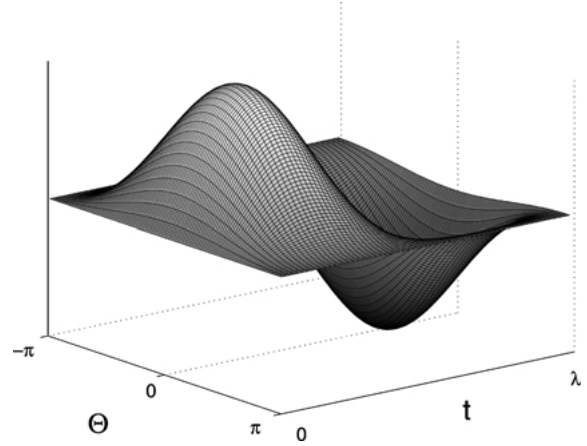


Figure 4. A representative  $f_{ign}(\Theta, t)$ , shown over one temporal period  $\lambda$ , and where the orientation hypercolumn of maximal stimulation is set at  $\Theta = 0$ .

set  $\theta = 0$  and drop its explicit dependence. Figure 4 shows a representative  $g_{ign}(\Theta, t)$  (reflecting Eq. (6)) over one temporal period, where the orientation of maximal stimulation is set at  $\Theta = 0$  and minimal at  $\Theta = \pm\pi$ .

Consider as the simplest model the *thresholded-linear* CG equations (22):

$$\begin{aligned} \langle m_P \rangle_t(\mathbf{x}) &= \langle \{I_{D,P}(\mathbf{x}, t) - g_{T,P}(\mathbf{x}, t)\}^+ \rangle_t \\ &= \langle \{f(\Theta(\mathbf{x}), t) + C_{PE} \cdot K_{PE} * \langle m_E \rangle_t(\mathbf{x}) \\ &\quad - C_{PI} \cdot K_{PI} * \langle m_I \rangle_t(\mathbf{x})\}^+ \rangle_t, \end{aligned} \quad (33)$$

for  $P = E, I$ . Here it is worth recalling Eq. (7), which implies that  $\langle f \rangle_t = \bar{f}$  is independent of  $\Theta$ . This implies that in the absence of nonlinearity—above, the thresholding  $\{\cdot\}^+$ —this model network could evince no orientation selectivity.

### The Special Case of Feed-Forward Inhibition

As a very constructive example, we specialize to the case of *feed-forward inhibition* by setting the interaction constants  $C_{EE} = C_{IE} = C_{II} = 0$ . In this case, the inhibitory firing rate  $\langle m_I \rangle_t$  is expressed directly in terms of the LGN drive:

$$\langle m_I \rangle_t = \langle f^+ \rangle_t(\Theta), \quad (34)$$

and is only a function of  $\Theta$ . For  $f$  as in Fig. 4, with  $f^+ \neq f$ ,  $\langle m_I \rangle_t(\Theta)$  will be maximal at  $\Theta = 0$  and decrease monotonically and symmetrically to its minima at  $\Theta = \pm\pi$ . This case yields for the excitatory firing

rate:

$$\langle m_E \rangle_t(\mathbf{x}) = \left\langle \left\{ f(\Theta(\mathbf{x}), t) - C_{EI} \times \int K_{EI}(\mathbf{x} - \mathbf{x}') \langle f^+ \rangle_t(\Theta(\mathbf{x}')) d^2 \mathbf{x}' \right\}^+ \right\rangle_t. \quad (35)$$

The geometry of firing rates and orientation selectivity follows from this expression. First, for  $f$  of the form shown in Fig. 4, the cortico-cortical inhibition,  $C_{EI} K_{EI} * \langle f^+ \rangle_t$ , decreases monotonically from right to left along the line  $y = 0$ . It then follows that  $\langle m_E \rangle_t$  increases along the ray  $\Theta = 0$  as the pinwheel center is approached. Crossing the center onto the ray  $\Theta = \pi$ , the firing rate jumps down discontinuously (while  $K_{EI} * \langle f^+ \rangle_t$  is continuous at the pinwheel center,  $\langle f^+ \rangle_t$  is not) and thence increases moving out along  $\Theta = \pi$ . This feature is roughly observed in the point-neuron simulations shown in Fig. 2, as well as in the full CG solutions, found numerically and discussed in the next section.

Now, consider excitatory CG-cells, both near and the far from the pinwheel center. In these two cases, the support of the spatial convolution in Eq. (35) relative to the spatial variation of preferred orientation leads to the following observations:

- *Far from the pinwheel center* Consider  $|\mathbf{x}| \gg L_{EI}$ . Equation (23) then yields

$$\int K_{EI}(\mathbf{x} - \mathbf{x}') \langle f^+ \rangle_t(\Theta(\mathbf{x}')) d^2 \mathbf{x}' \simeq \langle f^+ \rangle_t(\Theta(\mathbf{x})). \quad (36)$$

Thus, the cortico-cortical inhibition in the far-field reflects directly the LGN drive and is both selective and determined locally in  $\Theta$ .

- *Near the pinwheel center* For  $|\mathbf{x}| \ll L_{EI}$ ,

$$\begin{aligned} & \int K_{EI}(\mathbf{x} - \mathbf{x}') \langle f^+ \rangle_t(\Theta(\mathbf{x}')) d^2 \mathbf{x}' \\ & \simeq \int K_{EI}(\mathbf{x}') \langle f^+ \rangle_t(\Theta(\mathbf{x}')) d^2 \mathbf{x}' \\ & = \frac{1}{2\pi} \int_0^{2\pi} \langle f^+ \rangle_t(\Theta) d\Theta \equiv \langle f^+ \rangle_{t,\Theta}. \end{aligned} \quad (37)$$

This last identity uses the axisymmetry of the kernel  $K_{EI}(\mathbf{x})$  about  $\mathbf{x} = \mathbf{0}$ , which  $K_{EI}$  has unit integral and

which  $f$  depends spatially only on  $\Theta$ . Thus, the near-field cortico-cortical inhibition is determined nonlocally and is nonselective in  $\Theta$ .

These two expressions show clearly that far-neurons should be inhibited very differently from near-neurons: far-neurons receive inhibition from cells representing only a small range of orientation preferences, while near-neurons receive inhibition from neurons representing all orientation preferences. This difference of local versus global inhibition arises because only those inhibitory neurons that are spatially close to an excitatory neuron can inhibit it monosynaptically. This distance of influence is set by the axonal arbor of the inhibitory neuron and the dendritic arbor of the excitatory neuron. Far from the pinwheel center, only neurons of very similar orientation preferences lie within this circle of influence, whereas near the pinwheel center all angles of orientation preference lie within it (see Fig. 1). Such differences in the selectivity of cortico-cortical inhibition near and far from a pinwheel center are observed in our large-scale point neuron simulations (see McLaughlin et al., 2000, Fig. 6) and are studied further in the next section.

Inserting the above expressions into Eq. (35) produces the following expression for the firing rates of these two CG-cells:

$$\langle m_E \rangle_t(\Theta; far) \simeq \langle \{ f(\Theta, t) - C_{EI} \langle f^+ \rangle_t(\Theta) \}^+ \rangle_t \quad (38)$$

$$\langle m_E \rangle_t(\Theta; near) \simeq \langle \{ f(\Theta, t) - C_{EI} \langle f^+ \rangle_{t,\Theta} \}^+ \rangle_t. \quad (39)$$

From these formulas the mechanisms that cause the distinct spatial patterns of firing rate and orientation selectivity become apparent. Consider near and far CG-cells, both with preferred orientation  $\theta_{pref} = 0$  (or  $\Theta_{pref} = 0$ ) and with  $\theta_{orth}$  denoting orthogonal to preferred (or  $\Theta_{orth} = \pm\pi$ ). We begin with the inequality

$$\langle f^+ \rangle_t(\Theta_{orth}) \leq \langle f^+ \rangle_{t,\Theta} \leq \langle f^+ \rangle_t(\Theta_{pref}). \quad (40)$$

Note that the latter half of this inequality implies that inhibition at preferred orientation is larger for far CG-cells than for near CG-cells. This is consistent with the I&F simulations (McLaughlin et al., 2000, Fig. 6; Wielaard et al., 2001, Fig. 6) and with results of the next section. From Eqs. (38) and (39) it now follows

that

$$\langle m_E \rangle_t(\Theta_{pref}; near) \geq \langle m_E \rangle_t(\Theta_{pref}; far) \quad (41)$$

and that

$$\langle m_E \rangle_t(\Theta_{orth}; near) \leq \langle m_E \rangle_t(\Theta_{orth}; far). \quad (42)$$

Using the monotonicity of  $K_{EI} * \langle f^+ \rangle_t$ , among other things, shows the further ordering

$$\begin{aligned} \langle m_E \rangle_t(\Theta_{orth}; near) &\leq \langle m_E \rangle_t(\Theta_{orth}; far) \\ &\leq \langle m_E \rangle_t(\Theta_{pref}; far) \leq \langle m_E \rangle_t(\Theta_{pref}; near), \end{aligned} \quad (43)$$

with  $\langle m_E \rangle_t(\Theta_{pref}; near)$  being the system's highest firing rate and  $\langle m_E \rangle_t(\Theta_{orth}; near)$  the lowest. This ordering of the firing rates is apparent in the I&F simulations shown in Fig. 2 and in our full CG solutions (next section).

Inequalities (41) and (42) together suggest that the form of inhibition near the pinwheel center leads to increased modulation, relative to the far-field, in the orientation tuning curve. It is this trait that underlies the sharper selectivity found there. Further, the form of the inhibitory contribution to Eq. (35) implies that these differences in near and far-field selectivity should occur over a distance  $L_{EI}$  from the pinwheel center, as is observed in the full I&F point-neuron simulations and in our full CG solutions (next section).

Thus, in this case of feed-forward inhibition, coarse-grained analysis shows precisely that neurons near pinwheel centers are more selective for orientation than those far and that this property arises from the global inhibition in  $\Theta$  near the pinwheel centers—in contrast to the local inhibition in  $\Theta$  experienced by far neurons.

Finally, it is interesting that in this simple model, if  $f^+ = f$  so that  $\langle m_I \rangle_t = \bar{f}$  is independent of  $\Theta$ , then inhibition is everywhere the same, and there are no near/far differences in either firing rates or selectivity. This is a consequence of the phase averages becoming time averages for these drifting grating solutions and that inhibition is mimicking its unrectified LGN drive.

**A More General Case with Cortico-cortical Inhibition** Using the far- and near-field models, this comparison of near/far responses can be generalized to cases where the dominant inhibitory couplings are retained. That is, we compare the far-field model

$$\langle m_P \rangle_t(\Theta) = \langle \{f(\Theta, t) - C_{PI} \langle m_I \rangle_t(\Theta)\}^+ \rangle_t, \quad (44)$$

with the near-field model

$$\langle m_P \rangle_t(\Theta) = \langle \{f(\Theta, t) - C_{PI} \langle m_I \rangle_t(\Theta)\}^+ \rangle_t, \quad (45)$$

for  $P = E, I$ . Note that relative to the choice of synaptic weights in the full point-neuron simulations of McLaughlin et al. (2000), only the subdominant cortico-cortical excitatory couplings have been dropped ( $C_{EE} = C_{IE} = 0$ ). With this choice of parameters, the  $P = I$  equation for  $m_I$  is independent of  $m_E$  and is solved separately, while  $m_E$  is determined explicitly once  $m_I$  is given. We will examine only the nature of solutions to the implicit equations for  $m_I$ , noting that if  $C_{EI} = C_{II}$  then  $m_E = m_I$ .

For notational ease, we define  $b(\Theta) \equiv \langle m_I \rangle_t(\Theta)$  in Eq. (44),  $a(\Theta) \equiv \langle m_I \rangle_t(\Theta)$  in Eq. (45), and  $C = C_{II}$ . Then, defining

$$z(x; \Theta) = \langle \{f(\Theta, t) - C \cdot x\}^+ \rangle_t, \quad (46)$$

these inhibitory firing rates satisfy

$$b(\Theta) = z(b(\Theta); \Theta), \quad far \quad (47)$$

$$a(\Theta) = z(\langle a \rangle_\Theta; \Theta), \quad near. \quad (48)$$

The function  $z(x; \Theta)$  is strictly decreasing for  $x \leq \max_t f^+(\Theta, t)/C$  and is zero thereafter. The relations (47) and (48) have their own interesting properties:

- $\langle a \rangle_\Theta$  is determined by the scalar fixed-point equation

$$\langle a \rangle_\Theta = \langle (\langle a \rangle_\Theta; \Theta) \rangle_\Theta \equiv y(\langle a \rangle_\Theta). \quad (49)$$

This relation always has a unique, nonnegative solution. If  $f^+ \equiv 0$ , then  $\langle a \rangle_\Theta = 0$ . If  $f^+$  is not everywhere zero, then there exists  $\bar{x} > 0$  ( $\bar{x} = \max_{\Theta, t} f^+/C$ ) such that  $y(x)$  is positive and monotonically decreasing on the interval  $[0, \bar{x})$  and with  $y(x) = 0$  for  $x \geq \bar{x}$ . This implies that there is then a unique  $\langle a \rangle_\Theta > 0$ . These arguments use that  $\{a - b\}^+ = \{a^+ - b\}^+$  for  $b \geq 0$ .

- The relation  $b(\Theta) = z(b(\Theta); \Theta)$  is also a fixed-point relation, now to be solved for each  $\Theta$ . The same argument as above gives the existence of a unique, nonnegative solution. In further analogy to  $\langle a \rangle_\Theta$ , it also implies that for a fixed  $\Theta$ , if  $f^+$  is not everywhere zero in  $t$ , then  $b(\Theta) > 0$  (this feature is shared with Eq. (34)). This gives a telling difference between  $a(\Theta)$  and  $b(\Theta)$ . The same function  $f$

can yield both positive  $\langle a \rangle_\Theta$  and (everywhere) positive  $b(\Theta)$ , but because  $a(\Theta)$  is explicitly determined once  $\langle a \rangle_\Theta$  is specified,  $a(\Theta)$  will itself have zero sets from rectification. This feature of thresholded firing rates near the pinwheel center (i.e., in  $a(\Theta)$ ) but no thresholding far (i.e., in  $b(\Theta)$ ) is observed in both our CG solutions and point-neuron network simulations.

Now we use a graphical argument to show that these near/far CG solutions share the same near/far inequalities (41), (42), and (43), with the simpler “feed-forward inhibition” model. Again, consider Fig. 4, which shows  $f(\Theta, t)$  with the orientation of maximal stimulation at  $\Theta_{pref} = 0$ . Let  $\tilde{x} = \min_{\Theta, t} f(\Theta, t)/C = f(\tilde{\Theta}, \tilde{t})/C$  (which might be negative). Then for  $x \leq \tilde{x}$ ,  $f(\Theta, t) - C \cdot x \geq 0$  for all  $\Theta$  and  $t$ , and hence

$$y(x) = z(x; \Theta) = w(x) \equiv \bar{f} - C \cdot x,$$

using that  $\langle f \rangle_t = \bar{f}$  is independent of  $\Theta$ . Figure 5 shows  $y(x)$  and  $z(x; \theta)$  for several values of  $\Theta$  (here  $\tilde{x} = 0$ ) and in particular for  $\Theta_{pref} = 0$  and  $\Theta_{orth} = \pi$ . Consider first  $y(x)$  and  $z(x; \Theta_{pref})$ . Both break equality with  $w(x)$  for  $x > \tilde{x}$  since  $f(\Theta, t)$  and  $f(\Theta_{pref}, t)$  have the same global minimum (at  $(\tilde{\Theta} = \Theta_{pref}, \tilde{t})$ ). Let  $x$  be slightly above  $\tilde{x}$ . Then, since  $f(\Theta_{pref}, t) < f(\Theta, t)$

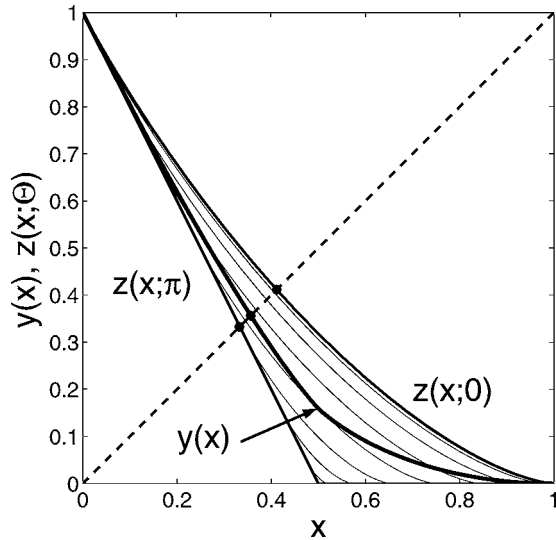


*Figure 5.* Solving the fixed-point Eqs. (47) and (49). The lower and upper bounding curves are  $z(x; \pi)$  and  $z(x; 0)$ , respectively, and the lighter curves are  $z(x; \Theta)$  at intermediate values of  $\Theta$ . The dark thick curve sandwiched between the bounding curves is  $y(x)$ . The dashed diagonal line is the curve  $y = x$ .

somewhere in a neighborhood of  $(\tilde{\Theta}, \tilde{t})$ , it is easy to see that  $y(x) < z(x; \Theta_{pref})$ . This separation is maintained to  $x = \tilde{x}$ , where  $y(x) = z(x; \Theta_{pref}) = 0$ , as  $f(\Theta, t)$  and  $f(\Theta_{pref}, t)$  share the global maximum. Since thresholding slows the rate of decrease of  $y(x)$ , we also have that  $y(x) > w(x)$ . Now consider  $z(x; \Theta_{orth})$ . Since  $f(\Theta_{orth}, t)$  has no  $t$  dependence (in our construction), we have directly  $z(x; \Theta_{orth}) = w(x)^+$ . Examination of Fig. 5 then implies directly that  $b_{min} = b(\Theta_{orth}) \leq \langle a \rangle_\Theta \leq b(\Theta_{pref}) = b_{max}$ . Now using that the function  $z$  is nondecreasing in its first argument gives

$$a(\Theta_{pref}) \leq b(\Theta_{pref}), \quad \text{and} \quad a(\Theta_{orth}) \leq b(\Theta_{orth}), \quad (50)$$

or as for the feed-forward inhibition model,

$$\begin{aligned} \langle m_E \rangle_t(\Theta_{orth}; \text{near}) &\leq \langle m_E \rangle_t(\Theta_{orth}; \text{far}) \\ &\leq \langle m_E \rangle_t(\Theta_{pref}; \text{far}) \leq \langle m_E \rangle_t(\Theta_{pref}; \text{near}). \end{aligned}$$

Again, these relations underly the increased modulation (in  $\theta$ ) of the firing rate, which manifests itself as lowered CVs near pinwheel centers.

We expect that much of the analysis presented in this section, using the thresholded-linear CG equations, survives when using more nonlinear CG systems such as Eqs. (16) and (17). This is because one central analytic property used here was the monotonicities of  $\mathcal{N}$  with respect to changes in excitatory and inhibitory conductance.

### 3.2.2. Numerical Solutions of the Full CG Equations.

We now turn to the study of the full CG system for drifting grating response, expressed in Eqs. (29) and (30). Solutions to Eq. (30) are found here by relaxation in time using Eq. (21) and seeking steady solutions  $\langle m_P \rangle_\phi$ . Here we use the simple choice of temporal kernel  $G_P(t) = \exp(-t/\tau_P)/\tau_P$  (for  $t > 0$ ). For this kernel, setting  $M_P = G_P * \langle m_P \rangle_\phi$  gives that  $\langle m_P \rangle_\phi = M_P - \tau_P \partial M_P / \partial t$ , and so Eq. (21) is transformed into a standard initial-value problem:

$$\begin{aligned} \tau_P \frac{\partial M_P}{\partial t}(\mathbf{x}, t) \\ = -M_P(\mathbf{x}, t) - \langle \mathcal{N}(g_{lgn}, S_{PP'} K_{PP'} * M_{P'}) \rangle_\phi, \\ P = E, I. \quad (51) \end{aligned}$$

This system is evolved forward using a second-order Adams-Bashforth integration method. While we are looking for steady solutions, in which case  $M_P = \langle m_P \rangle_t$ , seeking such solutions by temporal relaxation



can give information on the stability (or its lack) of such solutions, at least with respect to the specific choice of kernel  $G_P$ . (For example, this choice of  $G_P$  neglects differences in time-to-peak for excitatory versus inhibitory synaptic conductance changes.) More direct approaches to finding solutions using a Newton-Raphson method would converge in only a few iterations but would also require the inversion of large matrices, among other complications. Still, while the method used here is far from the most efficient, it is much more cost effective than use of a point-neuron simulation. As a point of comparison, producing a  $CV$  distribution using relaxation of the CG equations required two to three hours of CPU time on a single processor SGI (R10000 chip), versus two to three days on the same machine for the point neuron code.

For an 8 Hz drifting grating stimulus, Fig. 6 shows the distribution of time-averaged firing rates  $\langle m_{E,I} \rangle_t$  across the model cortical layer, found as solutions of

the full CG model, together with the distribution of  $CV[\langle m_{E,I} \rangle_t]$ , their circular variances. For this simulation, we have used the same synaptic weights  $S_{PP'}$  as in McLaughlin et al. (2000) and Wielaard et al. (2001), setting  $\tau_E = 0.003$  and  $\tau_I = 0.006$  (3 and 6 msec), and used  $32 \times 32$  excitatory and  $16 \times 16$  inhibitory CG-cells in each orientation hypercolumn. The spatial convolutions underlying the cortical interactions were evaluated using the fast fourier transform and the discrete convolution theorem. For computational efficiency, we use uniform densities for the noisy conductance densities  $\mathcal{F}_E$  and  $\mathcal{F}_I$  ( $g_E^0 = 6 \pm 6 \text{ s}^{-1}$ ,  $g_I^0 = 85 \pm 35 \text{ s}^{-1}$ ) to provide a rough approximation of the noisy conductances used in McLaughlin et al. (2000). For uniform distributions the two-dimensional distributional integrals in Eq. (29) can be reduced to integrals in only one variable through an exact integration.

The results shown in Fig. 6 should be compared with those shown in Fig. 2 from the I&F point-neuron

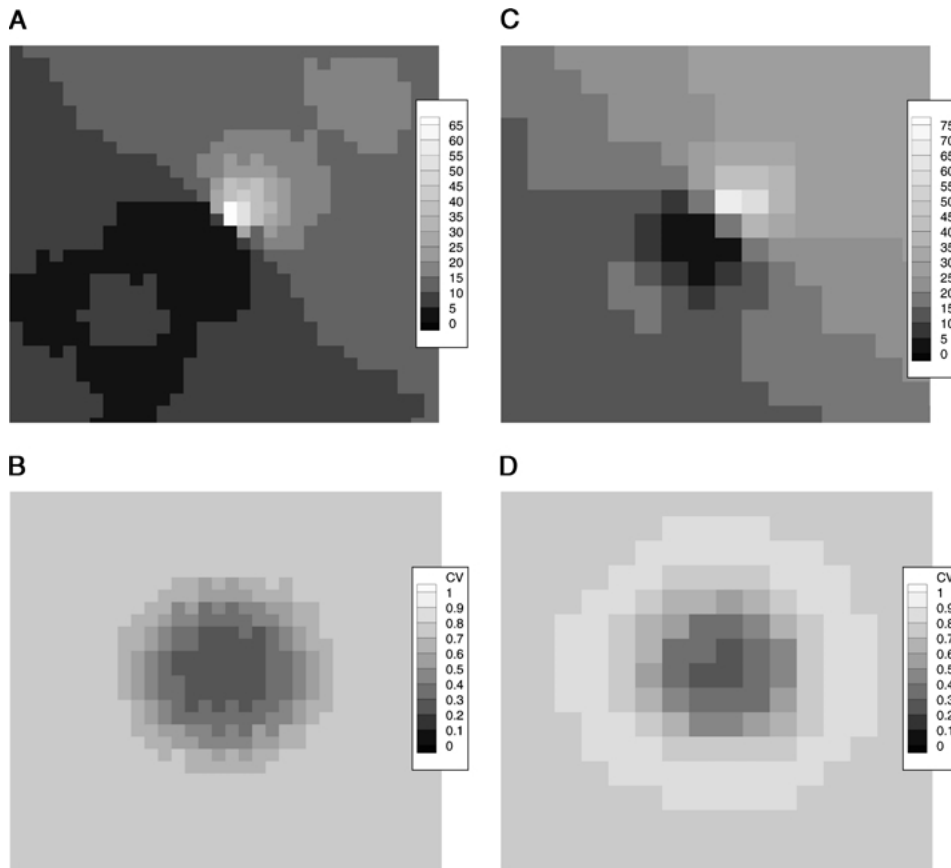


Figure 6. From the full CG network: The distribution across the model cortex of time-averaged firing-rates (A, excitatory; C, inhibitory) and of circular variance (B, excitatory; D, inhibitory) (see Fig. 2). Here, only one of the four orientation hypercolumns in the model is shown.

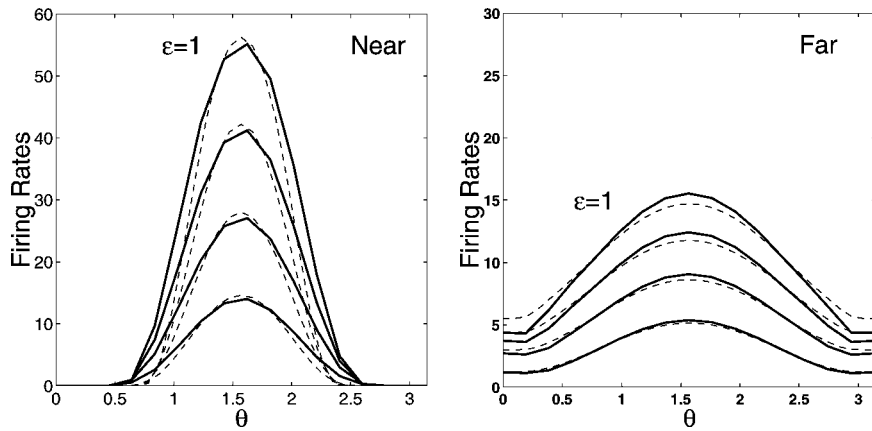


Figure 7. *Left*: Solid curves are orientation tuning curves for an excitatory neuron near the pinwheel center, for various contrasts ( $\epsilon = 1.0, 0.75, 0.50, 0.25$ ) from the full CG network (solid). The dashed curves are tuning curves gotten from Eq. (25), the near-field model. *Right*: Solid curves are tuning curves for an excitatory neuron far from the pinwheel center. Dashed curves are those gotten from the far-field approximation, Eq. (24). (see McLaughlin et al., 2000, Fig. 6).

simulations in McLaughlin et al. (2000), with which it shows good agreement in predicting higher firing rates near the pinwheel centers, as well as sharper orientation selectivity there. These differences in our model's near and far responses are illustrated further through Fig. 7, which shows the orientation tuning curves (at several contrasts) for two excitatory CG-cells, one near and one far from the pinwheel center. The sharper selectivity seen near the pinwheel center is consistent with the simulations in McLaughlin et al. (2000) and in accord with our mathematical analysis of the previous section. Note too the global positivity of the firing-rate curve of the far neuron, as is also predicted by this analysis.

Superimposed on the tuning curves of the near CG-cell in Fig. 6 are solutions to the near-field model given by Eq. (25). The near-field solution shows good fidelity to the near CG-cell response, showing comparable (and slightly sharper) selectivity and amplitude of firing. Superimposed on the tuning curves of the far CG-cell are those found from the far-field reduction expressed in Eq. (24). As both the far-field and near-field CG equations are considerably simpler than the full CG system, a solution  $\langle m_{E,I} \rangle_t(\theta; far)$  is found directly by Newton's method, using a continuation strategy. The agreement is quite good between the full- and far-field CG models, even though the modeled orientation hypercolumn is of finite width. These two figures reinforce the notion that important and distinct regions of the full CG model's spatial response—near and far from orientation singularities—can be understood through much reduced theoretical models.

Having found  $\langle m_{E,I} \rangle_t(\mathbf{x})$ , it is now straightforward to reconstruct *time-dependent* information—for example, firing rates from Eq. (29). Such data is shown in Figs. 8 and 9 for the near and far CG-cells, respectively, over one period of drifting grating stimuli set at each cell's preferred orientation (see Wielaard et al., 2001, Fig. 7). The first panel of both figures shows  $\langle m_E \rangle_t(t)$ , and their half-wave rectified wave-forms are those typically associated with simple cell responses to a drifting grating stimulus. The last three panels show the total conductance  $g_T$  and its two constituents, the excitatory and inhibitory conductances  $g_E$  and  $g_I$ . Recall that cortico-cortical contributions are time-invariant in our theory. Hence the fluctuations in  $g_T$  and  $g_E$  arise solely from the (tuned) fluctuations in  $g_{Ign}$ .

What is immediately clear is that under stimulation the total conductance is large and is dominated by its inhibitory part. As discussed in Shelley et al. (2001), this observation is consistent with recent experimental findings in cat primary visual cortex showing that under stimulation, conductances can rise to two to three times above their background values and are predominantly inhibitory and hence cortical in origin (Borg-Graham et al., 1998; Hirsch et al., 1998; Anderson et al., 2000). This observation is also consistent with an *a priori* assumption underlying our CG reduction: the time-scale associated with conductance (here  $\sim 2$  msec) is the smallest time-scale. Further, given the relative placements of the excitatory and inhibitory reversal potentials (here  $14/3$  and  $-2/3$ , respectively) to threshold (at 1),  $g_I$  necessarily exceeds  $g_E$  (here dominated by

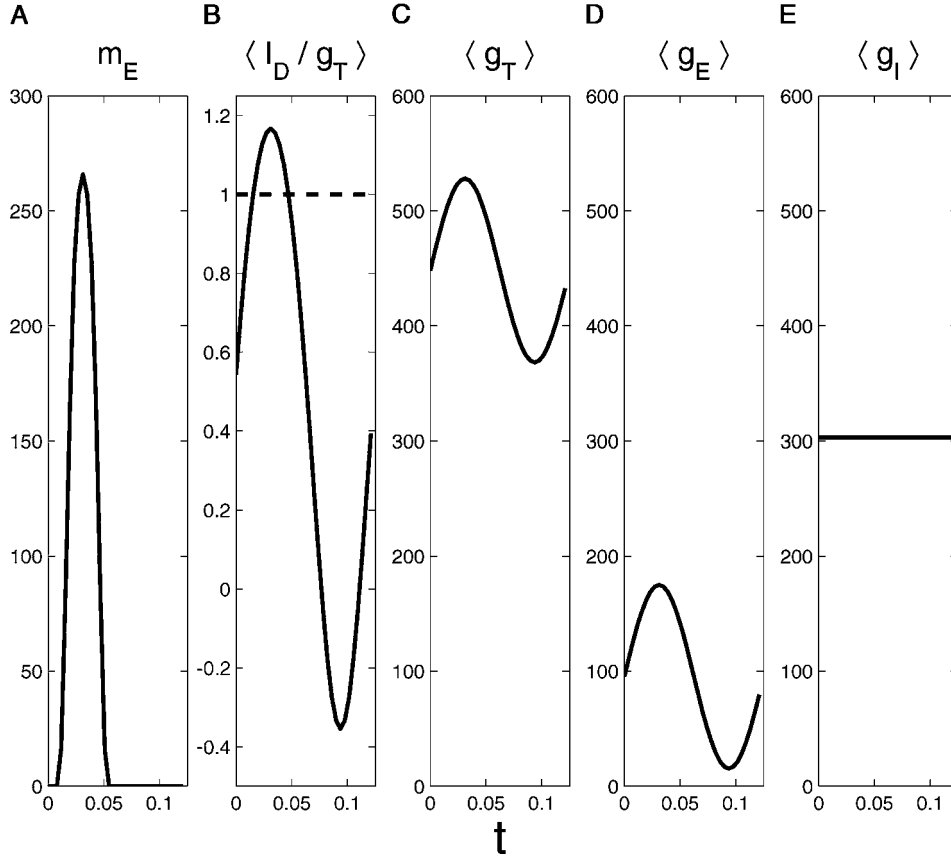


Figure 8. From the full CG network. **A:** The time-dependent firing-rate  $m_E(t)$  over a stimulus cycle for the near CG-cell in Fig. 7 for drifting grating stimulus at full contrast ( $\epsilon = 1$ ), and at preferred orientation. **B:** The expectation of the effective reversal potential  $V_S(t)$ . The dashed line is at the threshold to firing. **C, D, E:** The expectations of  $g_T$ ,  $g_E$ , and  $g_I$ , respectively (see Wielaard et al., 2001, Fig. 7).

$g_{lgn}$ ) so that inhibitory and excitatory membrane currents can be in balance and produce the good selectivity found in simple cells.

A second observation is that  $g_I$  is larger for the far CG-cell than for the near. This is explained and predicted through the analysis of the last section (see, for example, inequality (40) in combination with Eqs. (38) and (39)). It is this larger inhibition away from the pinwheel center that underlies the reduced firing rates, as is seen most directly through the dynamics of the potential  $V_S = I_D/g_T$  (the second panel in each figure), which in an overdamped neuron (described by Eq. (1)) approximates the cell's subthreshold potential  $v$ . For  $g_T$  dominated by  $g_I$ , and  $g_E$  by  $g_{lgn}$ , we have

$$V_S = \frac{V_E g_E(t) - |V_I| g_I}{g_R + g_E + g_I} \approx -|V_I| + V_E \frac{g_{lgn}(t)}{g_I}. \quad (52)$$

Thus, for each of these CG-cells, the potential follows closely the time-course of its LGN drive, but with

the amplitude of its modulation—particularly above threshold—controlled divisively by the inhibitory conductance. This yields simple cell responses in either case, with smaller firing rates away from the pinwheel center.

In Fig. 10 we investigate near/far differences underlying orientation selectivity. For a near CG-cell, panels A and B show the time-averaged threshold current

$$\langle I_D - g_T \rangle_t(\theta) = -g_R + (V_E - 1) \langle g_E \rangle_t(\theta) + (V_I - 1) \langle g_I \rangle_t(\theta) \quad (53)$$

and its inhibitory component  $(V_I - 1) \langle g_I \rangle_t(\theta)$ , respectively. Positivity of the threshold current is a necessary condition for cell firing. We see for this near CG-cell that both the threshold and inhibitory currents are quite unselective for orientation. As was analyzed in the previous section, it is this lack of orientation selectivity in near inhibition that gives sharper selectivity

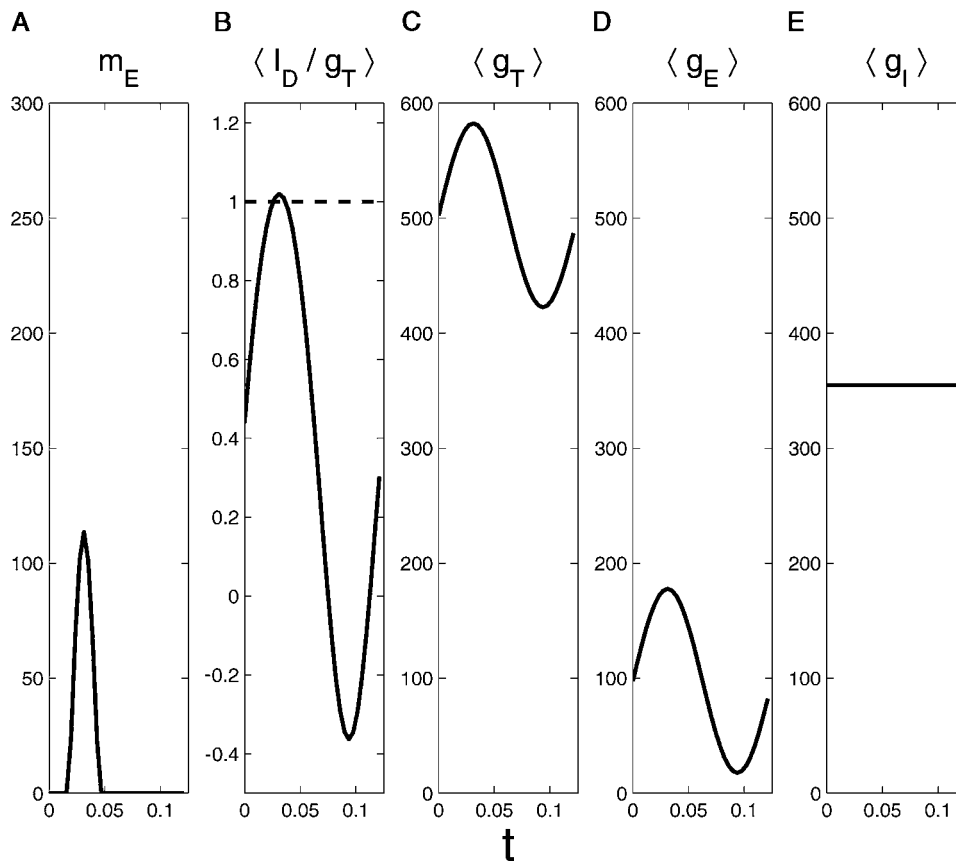


Figure 9. The same quantities as in Fig. 8 but for the far CG-cell in Fig. 7.

in cell response. That there is likewise little selectivity in the averaged threshold current follows from the fact both cortico-cortical conductances are unselective and that  $\langle g_{lgn} \rangle_t(\theta)$  is independent of  $\theta$ . The dashed curves are at  $\pm\sqrt{2}$  standard deviations, which in the absence of any contribution from the imposed noisy conductances would give exactly the envelope of temporal modulations of  $g_{lgn}$  in the threshold current. The size of the noisy contribution to the standard deviation is suggested by the inhibitory current, which contains no LGN contribution. We see in panel A that the mean threshold current is negative and that it is the predominantly LGN fluctuations that bring it above threshold.

For the far CG-cell, we see that the inhibitory current (panel C of Fig. 10) is now selective for orientation and, being the dominant, selective contribution, infers an orientation selectivity onto the mean threshold current. The noisy conductances now play an important role in bringing the threshold current above threshold (the upper dashed curve of panel C), and its weak modulation

underlies both the lower firing rates away from pinwheel centers and the lower selectivity.

These results are again in accord with the analysis of the previous section and with the analysis of the large-scale point-neuron simulations (see McLaughlin et al., 2000, Fig. 6). We now turn to considering the dependence of the CG-system on other parameters.

**Contrast Dependence** Contrast invariance in orientation selectivity is frequently cited as a common, though perhaps not universal, response property of primary visual cortex (Sclar and Freeman, 1982; Ben-Yishai et al., 1995; Somers et al., 1995; Troyer et al., 1998; Sompolinsky and Shapley, 1997; Anderson et al., 2000). One statement of contrast invariance is that there exists a function  $R(\theta)$  such that  $\langle m \rangle_t(\theta, \epsilon) = A(\epsilon)R(\theta)$ —that is, changes in stimulus contrast  $\epsilon$  simply rescale the amplitude of an underlying fundamental tuning curve  $R(\theta)$  and so do not change the “tuning width.” We note that there are not as yet physiological data addressing laminar differences in this selectivity

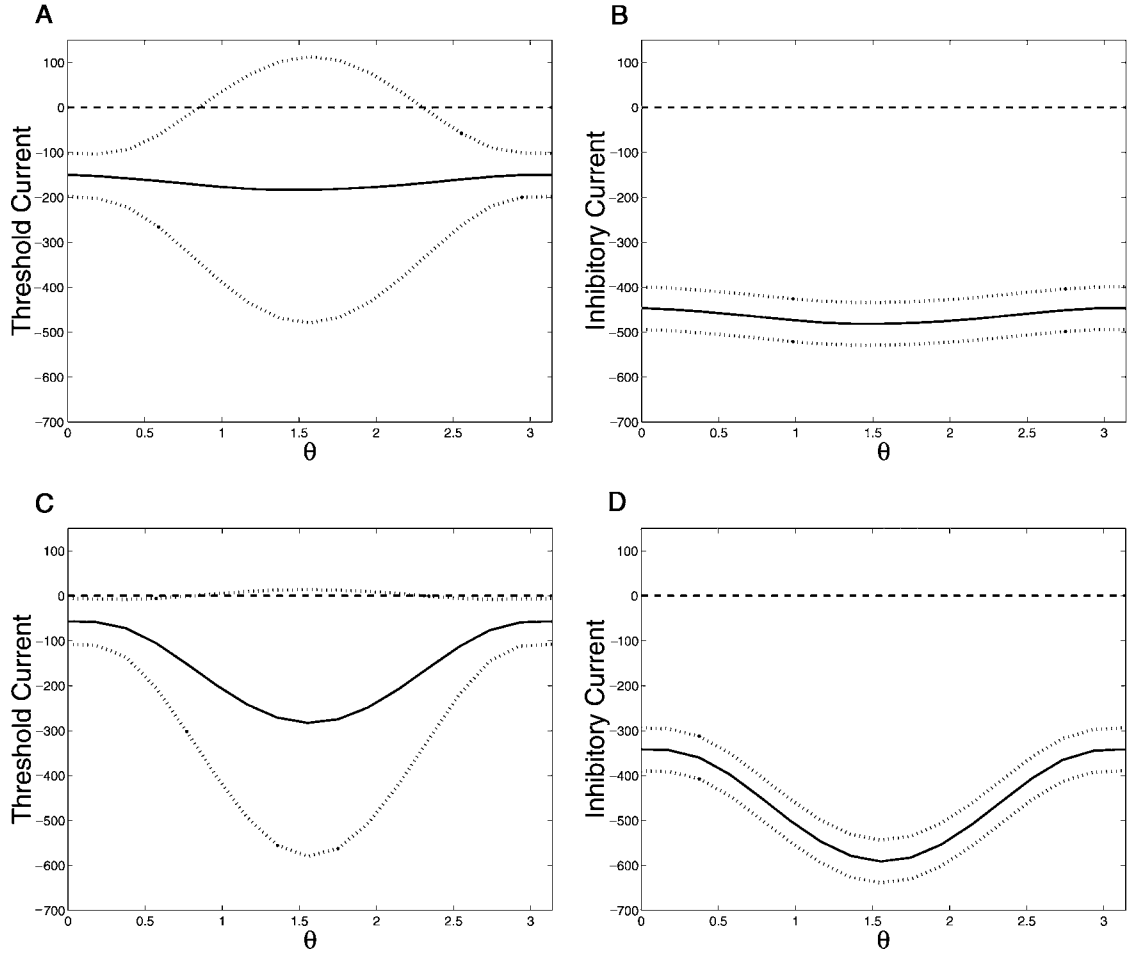


Figure 10. From the full CG network, the time-averaged threshold and inhibitory currents for a near CG-cell (panels A and B) and for a far CG-cell (panels C and D), as a function of  $\theta$ . The dashed curves are at  $\pm\sqrt{2}$  standard deviations (see McLaughlin et al., 2000, Fig. 6).

property and in particular whether contrast invariance is a common feature of  $4C\alpha$  of macaque V1.

Examination of the near and far tuning curves in Fig. 7 suggests that, in the model, contrast invariance is a feature of selectivity near the pinwheel center but much less so away away from the center. In the context of circular variance, contrast invariance would imply that  $CV[\langle m \rangle_t] = CV[R]$  or that  $CV$  is independent of  $\epsilon$ . Figure 11 shows  $CV[\langle m_E \rangle_t]$  from the full CG system, for four contrasts,  $\epsilon = 0.25, 0.50, 0.75$ , and  $1.0$ , measured along a horizontal line cutting across an orientation hypercolumn and through its pinwheel center. Again, Fig. 11 shows that the model produces a region of contrast invariant tuning localized near the orientation center.

What is the basis for this observed contrast invariance and its near/far differences? Though it is only a

partial explanation, it is easy to see that within any of the CG models, contrast invariance emerges at sufficiently high contrast. Consider a “large” LGN forcing  $g_{lgn}(\mathbf{x}, t) = \delta^{-1}q(\mathbf{x}, t)$ , with  $0 < \delta \ll 1$ , within the fully nonlinear CG model (30), and seek likewise large solutions  $\langle m_P \rangle_t = \delta^{-1}R_P$ . At leading order in  $\delta^{-1}$ , the leakage and stochastic conductances drop out, and the  $R_P$  satisfy the equations

$$R_P(\mathbf{x}) = \langle \mathcal{N}(q(\mathbf{x}, t), S_{PP'}K_{PP'} * R_{P'}(\mathbf{x})) \rangle_t, \quad (54)$$

where  $\mathcal{N}$  is defined as in Eq. (17),

$$\mathcal{N} = \frac{-g_T}{\log[1 - g_T/I_D]} \quad \text{for } I_D > g_T \text{ and 0 otherwise,} \quad (55)$$

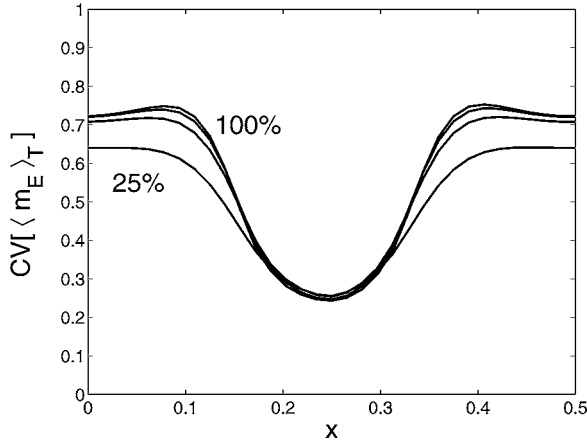


Figure 11. From the full CG network, a cross-section of the CV distribution, cutting across a hypercolumn, for contrasts  $\epsilon = 0.25, 0.5, 0.75,$  and  $1.0$ .

but with

$$g_{T,P}(\mathbf{x}, t) \equiv q(\mathbf{x}, t) + \sum_{P'} S_{PP'} K_{PP'} * R_{P'}(\mathbf{x})$$

$$I_{D,P}(\mathbf{x}, t) \equiv V_E q(\mathbf{x}, t) + \sum_{P'} V_{P'} S_{PP'} K_{PP'} * R_{P'}(\mathbf{x}).$$
(56)

Such large solutions will be contrast invariant. In the case of uniform cortico-cortical inhibition with only LGN excitation, Ben-Yishai et al. (1995) investigated such large-contrast solutions in their study of a thresholded-linear mean-field model.

We have numerically constructed solutions  $R_P$  to these equations for the near- and far-field models, and Fig. 12 shows their comparison with the finite contrast far- and near-field solutions shown in Fig. 6. Here we have rescaled all tuning curves to have unit maximum. First, the near-field tuning curves are rather well-described by  $R_E(\theta; near)$ . Indeed, a close examination reveals that this range of contrasts is part of a monotonic approach to  $R_E$  with increasing contrast but with substantial nonlinear difference components still present. The far-field behavior is much different. For the contrasts shown, the far-field solutions are far from a range of uniform behavior with respect to  $R_I(\theta; far)$ , except perhaps in a neighborhood of the preferred orientation.

Contrast invariance is a global property of the firing-rate curve, and to see contrast invariance through this large-contrast avenue, large  $O(\delta^{-1})$  amplitudes must be realized everywhere in  $\theta$  (unless the deficient region is thresholded and so is “out-of-sight”). The approach to contrast-invariant behavior is aided by the ability of the solution to sample the large temporal fluctuations of the LGN drive. For the far-field model, this is possible near the preferred orientation  $\theta_{pref}$  but not at  $\theta_{orth}$ , where there are no such fluctuations. For the near-field model, the solution is determined globally in  $\theta$ —for example, by the determination of  $\langle a \rangle_{\ominus}$  through Eq. (49) in the previous analysis of the thresholded-linear version. Thus, for the near-field model, the temporal fluctuations are felt globally in  $\theta$ , yielding a faster approach to large-contrast behavior.

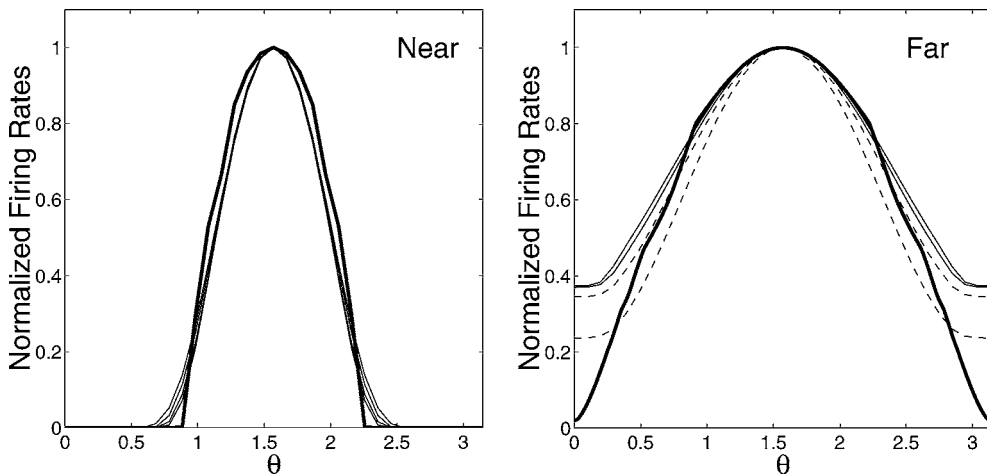


Figure 12. *Left:* A comparison of near-field tuning curves at for contrasts  $\epsilon = 0.25, 0.5, 0.75, 1.0$  with the large contrast tuning curve  $N_E$  for the near-field model (heavy solid curve). *Right:* The same as in the left figure but for the far-field model. In this case, the dashed curves are for  $\epsilon = 0.25$  (lowest) and  $0.5$ . The two solid curves are for  $\epsilon = 0.75$  and  $1.0$ .

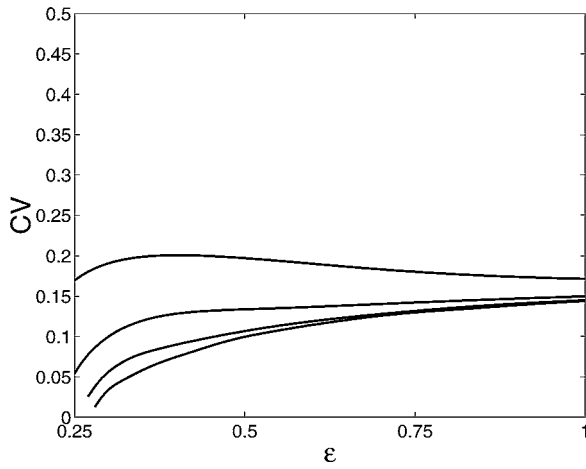


Figure 13. For the near-field model,  $CV[\langle m_E \rangle_t]$  as a function of contrast  $\epsilon$ , as the amplitude of fluctuation of the stochastic conductances about their means is successively halved, leading to successively lower CV curves.

This argument only explains response at large contrast. We find that the propagation of contrast invariant response to lower contrast is greatly aided by the presence of the stochastic conductance contributions. Figure 13 shows  $CV[\langle m_E \rangle_t]$  for the near-field model as the range of the noisy fluctuations is successively halved. At higher contrast, near  $\epsilon = 1$ , these fluctuations play a minor role in determining the CV. For small fluctuations, as the contrast is reduced the CV decreases monotonically toward zero due to the “iceberg effect” (that is, the lowering of firing-rate curve through a fixed threshold), yielding smaller responses over a narrowing range (see Sompolinsky and Shapley, 1997). On the other hand, in the presence of stronger noisy fluctuations, the firing-rate still decreases as the contrast is lowered, but the noisiness keeps the network activity above threshold over a broader range, yielding more contrast-invariant responses. This result

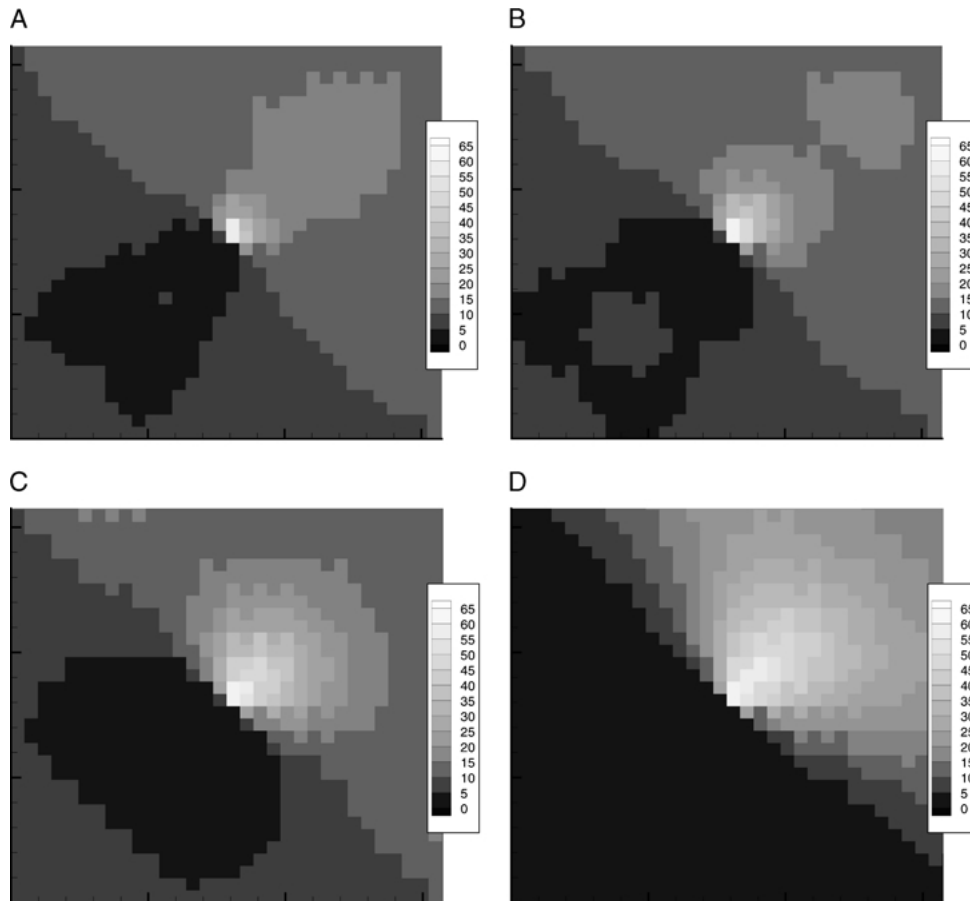


Figure 14. From the full CG network, the spatial distribution of time-averaged excitatory firing-rates for four different inhibitory coupling lengths. **A:**  $L_I \approx 70 \mu\text{m}$ , **B:**  $100 \mu\text{m}$  (the standard value), **C:**  $200 \mu\text{m}$ , and **D:**  $400 \mu\text{m}$ .

is consistent with recent observations of Anderson et al. (2000) on the effects of noise in orientation tuning in cat visual cortex.

**Length-Scale Dependencies** One important question is what determines the scale of the region of sharper selectivity in our model. Given the strong inhibition, a reasonable guess is the axonal length-scale of inhibition, which we estimate from the anatomy to have a radius of  $r_A^I = 100 \mu\text{m}$ , which with a dendritic tree radius of  $r_D^{I,E} = 50 \mu\text{m}$  sets the two length-scales  $L_I = L_{IE} = L_{II} \approx 100 \mu\text{m}$ .

Figure 14 shows the associated distributions of firing-rates  $\langle m_E \rangle_t$  for four different values of  $r_A^I$  (50, 100, 200, 400  $\mu\text{m}$ , giving approximately 70, 100, 200, 400  $\mu\text{m}$  for  $L_I$ ). As was suggested by our analysis of the previous section, as  $L_I$  is increased, the region of higher firing-rates increase further outward from the orientation singularity with increasing  $L_I$ . Indeed,  $\langle m_E \rangle_t$  near the pinwheel center changes very little with increasing  $L_I$ .

Figure 15 shows the spatial distribution of  $CV[\langle m_E \rangle_t]$ , for these four coupling lengths, along a horizontal line cutting through pinwheel center. Clearly, the region of sharpest selectivity increases with  $L_I$ , and indeed at the largest diameter that more than spans the hypercolumn, the degree of selectivity has become uniform. The width of the sharp selectivity region scales very well with  $2L_I$ , the radius of inhibitory input to the excitatory population, up to the point where it exceeds the hypercolumn width.

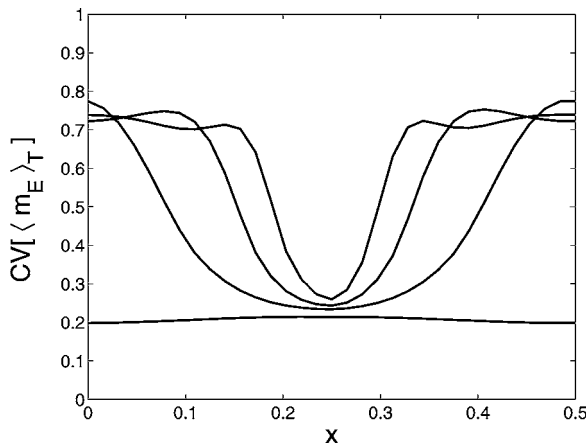


Figure 15. A cross-section of the CV distribution, cutting across a hypercolumn, for the four inhibitory coupling lengths in Fig. 14.

#### 4. Discussion

In this work we described a reduction of our large-scale I&F neuronal network model to a simpler, spatially coarse-grained system for firing-rates of neuronal subpopulations. A crucial element in the mathematical structure of the CG model is the appearance of phase-averaged firing-rates in the cortico-cortical conductances (see Eq. (13)). This phase averaging arises from the assumption that the preferred spatial phase of neurons presynaptic to a given cell was randomly distributed from a broad distribution. A consequence of this interpretation of cortical architecture—i.e., coupling is nonspecific in phase—is the prediction that for drifting grating stimuli, cycle-averaged cortico-cortical conductances should be time invariant, as has been approximately observed in our large-scale I&F simulations (Wielaard et al., 2001). The phase averaging of inhibition-dominated, cortico-cortical conductances was also a crucial element to our I&F network model, producing simple cell responses to contrast reversal stimuli (Wielaard et al., 2001). We note that phase-averaging is inherent in a recurrent network model of complex cells due to Chance et al. (1999), which also presumes simple cell inputs, as might be generated by a model such as ours.

In this aspect, our model is very different from “push-pull” models (Palmer and Davis, 1981; Tolhurst and Dean, 1990) that posit a direct or indirect phase-sensitive inhibition from the LGN. Direct inhibition from LGN to cortical neurons is ruled out by anatomy; LGN-to-cortex inhibitory synapses do not exist. One might attempt to preserve the “push-pull” concept by postulating that disynaptic inhibition from inhibitory neurons in the cortex could provide phase-sensitive inhibition, as has been instantiated in the model of Troyer et al. (1998), where cortical couplings are explicitly phase-specific.

There is recent experimental evidence bearing on these different conceptions of cortical architecture. From measurements of simple cell responses to drifting gratings, Anderson et al. (2000) infer that the temporal modulation of synaptic inhibition in opposition to the modulation of synaptic excitation is indicative of push-pull interactions between inhibition and excitation. However, scrutiny of their measurements indicates also that there usually is a large, phase-insensitive component of the inhibitory conductance, consistent with the phase-insensitive inhibition that is observed in our model’s response to drifting gratings (see Wielaard



et al., 2001, Figs. 7, 9). Further, other direct intracellular measurements by Borg-Graham and colleagues (Borg-Graham et al., 1998) indicate that inhibition in simple cells is more often spatial phase-insensitive than phase-sensitive (or “push-pull”)—as Borg-Graham et al. indeed noted. Our model produces unmodulated cortical inhibition in response to drifting gratings because neurons are excited by inhibitory neighbors of different spatial phase preference. Perhaps the real cortex has inhibitory conductances that are neither wholly phase-insensitive as in our model nor wholly phase-sensitive as envisioned in push-pull models but have a phase sensitivity somewhere between all or none. In any case, one point of mathematical and simulation analysis is that the differences that arise from these distinct models of cortical architecture are sharply delineated.

For drifting grating stimuli we also used the CG reduction to understand, through mathematical analysis and simulation, the mechanisms underlying the firing-rate and orientation-selectivity patterns observed in our I&F network (McLaughlin et al., 2000). This analysis showed that it is an interaction between the pinwheel structure of the preferred orientation mapping and the isotropic architecture that produces greater orientation selectivity near pinwheel centers. That cortico-cortical inhibition is strong and that its coupling length-scale is below the hypercolumn size are key to this analysis. We found other near/far differences in the properties of orientation selectivity, in particular the degree of invariance to changes in contrast. We found contrast invariance was most readily achieved in the pinwheel center and showed also the salutary effect of noise in maintaining it. This latter point is consistent with a recent study by Anderson et al. (2000).

Using tetrode measurements combined with optical imaging, Maldonado et al. (1997) have sought to determine experimentally whether orientation selectivity differs near and far from pinwheel centers (see also Das and Gilbert, 1999). They used the half-width of a Gaussian fit as an estimate for a tuning width and reported no substantial differences in tuning near and far from pinwheel centers. However, their study was in cat striate cortex, and the laminar location of the recorded cells was unknown. Our network is built on the architecture of input layer  $4C\alpha$  of Macaque; if truly present, such near/far differences may not survive in other layers due to spread of axonal projections from  $4C\alpha$ . Ours is also a network of simple cells. Complex cells make up a large fraction of selective cells in visual cortex (Ringach et al., 2001) and may have different

tuning properties from simple cells relative to pinwheel centers.

We also demonstrated the ability of the coarse-grained system to capture the salient features of our I&F point-neuron simulations but at a far lower computational cost. This is an important consideration as we seek to understand neuronal network dynamics at greater spatial, temporal, and functional scales. We are currently investigating how coarse-grained models can replace, or be integrated, with finer-scale dynamical representations such as point-neurons.

### Acknowledgments

We thank Louis Tao and David Cai for useful conversations, Gary Blasdel for his permission to reproduce his published data, and Estarose Wolfson for technical assistance in the preparation of figures. The authors especially thank Robert Shapley for his ongoing and fruitful collaboration, as well as critical guidance. The authors acknowledge the support of National Science Foundation Grants DMS-9971813 (DM) and DMS-9707494 (MS).

### References

- Anderson J, Carandini M, Ferster D (2000) Orientation tuning of input conductance, excitation, and inhibition in cat primary visual cortex. *J. Neurophysiol.* 84: 909–926.
- Anderson J, Lampl I, Gillespie D, Ferster D (2000) The contribution of noise to contrast invariance of orientation tuning in cat visual cortex. *Science* 290: 1968–1972.
- Azouz R, Gray CM, Nowak LG, McCormick DA (1997) Physiological properties of inhibitory interneurons in cat striate cortex. *Cereb. Cortex* 7: 534–545.
- Benardete E, Kaplan E (1999) The dynamics of primate M retinal ganglion cells. *Visual Neurosci.* 16: 355–368.
- Ben-Yishai R, Bar-Or R, Sompolinsky H (1995) Theory of orientation tuning in the visual cortex. *Proc. Nat. Acad. Sci. USA* 92: 3844–3848.
- Blasdel G (1992) Differential imaging of ocular dominance and orientation selectivity in monkey striate cortex. *J. Neurosci.* 12: 3115–3138.
- Bonhoeffer T, Grinvald A (1991) Iso-orientation domains in cat visual cortex are arranged in pinwheel like patterns. *Nature* 353: 429–431.
- Borg-Graham L, Monier C, Fregnac Y (1998) Visual input evokes transient and strong shunting inhibition in visual cortical neurons. *Nature* 393: 369–373.
- Bressloff P, Coombes S (2000) Dynamics of strongly coupled spiking neurons. *Neural Comput.* 12: 91–129.
- Callaway E (1998) Local circuits in primary visual cortex of the macaque monkey. *Ann. Rev. Neurosci.* 21: 47–74.

- Callaway E, Wiser A (1996) Contributions of individual layer 2 to 5 spiny neurons to local circuits in macaque primary visual cortex. *Visual Neurosci.* 13: 907–922.
- Chance F, Nelson S, Abbott LF (1999) Complex cells as cortically amplified simple cells. *Nature Neurosci.* 2: 277–282.
- Das A, Gilbert C (1999) Topography of contextual modulations mediated by short-range interactions in primary visual cortex. *Nature* 399: 655–661.
- DeAngelis G, Ghose R, Ohzawa I, Freeman R (1999) Functional micro-organization of primary visual cortex: Receptive field analysis of nearby neurons. *J. Neurosci.* 19: 4046–4064.
- De Valois R, Albrecht D, Thorell L (1982) Spatial frequency selectivity of cells in macaque visual cortex. *Vision Res.* 22: 545–559.
- Ermentrout GB (1994) Reduction of conductance based models with slow synapses to neural networks. *Neural Comput.* 6: 679–695.
- Feller W (1968) *An Introduction to Probability Theory and Its Applications.* John Wiley, New York.
- Ferster D, Chung S, Wheat H (1996) Orientation selectivity of thalamic input to simple cells of cat visual cortex. *Nature* 380: 249–252.
- Fitzpatrick D, Lund J, Blasdel G (1985) Intrinsic connections of macaque striate cortex. Afferent and efferent connections of lamina 4C. *J. Neurosci.* 5: 3329–3349.
- Gerstner W (1995) Time structure of the activity in neural network models. *Phys. Rev. E* 51: 738–758.
- Gibson J, Beierlein M, Connors B (1999) Two networks of electrically coupled inhibitory neurons in neocortex. *Nature* 402: 75–79.
- Hansel D, Sompolinsky H (1998) *Modeling Feature Selectivity in Local Cortical Circuits.* MIT Press, Boston, MA. pp. 499–567.
- Hirsch J, Alonso JM, Reid R, Martinez L (1998) Synaptic integration in striate cortical simple cells. *J. Neurosci.* 15: 9517–9528.
- Jagadeesh B, Wheat H, Kontsevich L, Tyler C, Ferster D (1997) Direction selectivity of synaptic potentials in simple cells of the cat visual cortex. *J. Neurophysiol.* 78: 2772–2789.
- Knight B, Manin D, Sirovich L (1996) Dynamical models of interacting neuron populations. In: Gerf E, ed. *Symposium on Robotics and Cybernetics: Computational Engineering in Systems Applications.* Cite Scientifique, Lille, France.
- Laing C, Chow C (2001) Stationary bumps in networks of spiking neurons. *Neural Comput.* 13: 1473–1494.
- Lund JS (1987) Local circuit neurons of macaque monkey striate cortex: Neurons of laminae 4C and 5A. *J. Comp. Neurology* 257: 60–92.
- Maldonado P, Godecke I, Gray C, Bonhoeffer T (1997) Orientation selectivity in pinwheel centers in cat striate cortex. *Science* 276: 1551–1555.
- McLaughlin D, Kovacic G (2001) Private communication.
- McLaughlin D, Shapley R, Shelley M, Wielaard J (2000) A neuronal network model of macaque primary visual cortex (V1): Orientation selectivity and dynamics in the input layer 4C $\alpha$ . *Proc. Natl. Acad. Sci. USA* 97: 8087–8092.
- Nykamp D, Tranchina D (2000) A population density method that facilitates large-scale modeling of neural networks: Analysis and application to orientation tuning. *J. Comput. Neurosci.* 8: 19–50.
- Nykamp D, Tranchina D (2001) A population density method that facilitates large-scale modeling of neural networks: Extension to slow inhibitory synapses. *Neural Comput.* 13: 511–546.
- Palmer L, Davis T (1981) Receptive-field structure in cat striate cortex. *J. Neurophysiol.* 46: 260–276.
- Pugh M, Ringach D, Shapley R, Shelley M (2000) Computational modeling of orientation tuning dynamics in V1 neurons. *J. Comp. Neurosci.* 8: 143–159.
- Reid RC, Alonso JM (1995) Specificity of monosynaptic connections from thalamus to visual cortex. *Nature* 378: 281–284.
- Ringach D, Hawken M, Shapley R (1997) Dynamics of orientation tuning in macaque primary visual cortex. *Nature* 387: 281–284.
- Ringach D, Shapley R, Hawken M (2001) Diversity and laminar dependence of orientation selectivity in simple and complex cells of macaque v1. *J. Neurosci.* 21(14).
- Sclar G, Freeman R (1982) Orientation selectivity in the cat's striate cortex is invariant with stimulus contrast. *Exp. Brain Res.* 46: 457–461.
- Shapley R, Reid C (1998) Private communication.
- Shelley M, McLaughlin D, Cai D (2001) Point neuron and mean firing rate models of primary visual cortex.
- Shelley M, McLaughlin D, Shapley R, Wielaard J (2001) The high conductance state caused by visual stimulation in a large-scale computational model of the visual cortex: An emergent separation of time scales.
- Somers D, Nelson S, Sur M (1995) An emergent model of orientation selectivity in cat visual cortical simple cells. *J. Neurosci.* 15: 5448–5465.
- Sompolinsky H, Shapley R (1997) New perspectives on the mechanisms for orientation selectivity. *Current Opinion in Neurobiol.* 7: 514–522.
- Tolhurst D, Dean A (1990) The effects of contrast on the linearity of spatial summation of simple cells in the cat's striate cortex. *Exp. Brain Res.* 79: 582–588.
- Treves A (1993) Mean field analysis of neuronal spike dynamics. *Network* 4: 259–284.
- Troyer T, Krukowski A, Priebe N, Miller K (1998) Contrast invariant orientation tuning in cat visual cortex with feedforward tuning and correlation based intracortical connectivity. *J. Neurosci.* 18: 5908–5927.
- Wielaard J, Shelley M, Shapley R, McLaughlin D (2001) How simple cells are made in a nonlinear network model of the visual cortex. *J. Neurosci.* 21(14): 5203–5211.
- Wilson H, Cowan J (1973) A mathematical theory of the functional dynamics of cortical and thalamic nervous tissue. *Kybernetik* 13: 55–80.